



Abstract

This manuscript presents the internal facies architecture of the sediment in the upper layers of the Sefidrud delta, located along the south Caspian Sea coast. The delta lies between the subsiding southern basin and the uplifting Elburz Mountains, with its sharp topography shaped by several faults. It features a fine-grained, large Gilbert-type delta, primarily significant for paleoenvironmental studies and oil exploration. The modern Sefidrud delta serves as an analogue for predictive stratigraphical and sedimentological models of steep ancient deltas affected by rapid base-level changes and transversal faults. This study enhances the understanding of facies distribution and three-dimensional geometry in fine-grained, high-gradient Gilbert-type deltas. The analysis reveals various sedimentary structures indicative of dynamic depositional environments. The upper delta plain presents complex interleaving of fluvial and tidal deposits, where sedimentation is largely dominated by riverine processes and influenced by episodic flooding events. This interplay is evident in the sedimentary facies that transition from sand-rich, channel-fill deposits to finer, more overbank sediments. Palynological data further support the interpretation of a variable paleoenvironment, suggesting alternating periods of marine and freshwater influence consistent with base-level fluctuations. In contrast, the steep delta front exhibits distinctive features, such as coiffed embankments and avalanche deposits, which signify rapid sediment delivery from the deltaic system. The high-angle accumulations demonstrate the energetic conditions that govern deposition in such high-gradient settings, where sediment bypass is promoted by the steep slope.



Morphology of the Sefidrud Delta (Southwest Caspian Sea): a tectonically-driven Gilbert delta

ISBN : 978-622-8423-22-7



9 786228 423227

2024

UCCGHA 028

2024

**Morphology of the Sefidrud
Delta (Southwest Caspian Sea):
a tectonically-driven Gilbert
delta**



| | |
|---------------------|---|
| سرشناسه | : حقانی، صفیه، ۱۳۵۰- -Haghani, Safiyeh, 1971 |
| عنوان و نام پدیدآور | Morphology of the sefidrud delta (southwest caspian sea): a tectonically- driven Gilbert delta[Book]/ author Safiyeh Haghani...[et al.]; employer Brunel University London, CEREGE, Technopôle de l'Arbois- Méditerranée, Institute for Ecosystem Research, Kiel University, Laboratory for Climate Sciences and the Environment, Birkbeck University, Iranian National Institute for Oceanography and Atmospheric Science (INIOAS), Research Institute for Earth Sciences, Geological Survey of Iran; summarized and translated into English Manouchehr Ghorashi; with cooperation UNESCO Chair on Coastal Geo-Hazard Analysis. |
| مشخصات نشر | : تهران: نشر خزه، ۱۴۰۲ = ۲۰۲۴ م. |
| مشخصات ظاهری | : ۱۰۴ ص؛ ۱۵ × ۲۱ سم. |
| شابک | : 978-622-8423-22-7 |
| وضعیت فهرست نویسی | : فیپا |
| یادداشت | : زبان: انگلیسی. |
| یادداشت | : عنوان: مورفولوژی دلتای سفیدرود (جنوب غرب دریای کاسپین): دلتای تکتونیک- محور گیلبرت. |
| یادداشت | : Authors: Safiyeh Haghani, Suzanne A.G. Leroy, Ingmar Björn Unkel, Jean Louis Reyss, Charlie S. Bristow, Hamid A.Z. Lahijani, Abdolmajid Naderi Beni, Hamid Nazari, Mohammad Reza Ensani |
| موضوع | : دلتای رودخانه، نرخ رسوب، حوضه خزر جنوبی، دلتای گیلبرت، نیم رخ لرزه ای، ژئوشیمی، پالینولوژی |
| موضوع | : River delta, sedimentation rate, South Caspian Basin, Gilbert delta, seismic profile, geochemistry, palynology |
| شناسه افزوده | : حقانی، صفیه، ۱۳۵۰- |
| شناسه افزوده | : Haghani, Safiyeh, 1971- |
| شناسه افزوده | : کرسی یونسکو مخاطرات زمین شناختی ساحلی |
| شناسه افزوده | : UNESCO Chair on Coastal Geo-Hazard Analysis |
| شناسه افزوده | : پژوهشکده علوم زمین |
| شناسه افزوده | : Research Institute of Earth Sciences |
| رده بندی کنگره | : GB۴۳۸ |
| رده بندی دیویی | : ۴۰۹۵۵۲۳/۵۵۱ |
| شماره کتابشناسی ملی | : ۹۸۳۰۶۱۹ |

**Morphology of the Sefidrud
Delta (Southwest Caspian Sea):
a tectonically-driven Gilbert
delta**

Author:

Safiyeh Haghani





UNESCO Chair on
Coastal Geo-Hazard Analysis
Research Institute for Earth Sciences
Geological Survey of Iran



اطلاعات گزارش

عنوان: مورفولوژی دلتای سفیدرود (جنوب غرب دریای کاسپین): دلتای تکتونیک-محور
گیلبرت
مجری: دانشگاه بروئل لندن، CEREGE، تکنوپل لاربویس مدیترانه، موسسه تحقیقات
اکوسیستم، دانشگاه کیل، آزمایشگاه علوم آب و هوا و محیط زیست، دانشگاه بیرکبک،
پژوهشگاه ملی اقیانوس شناسی و علوم جوی ایران (INIOAS)، پژوهشکده علوم زمین،
سازمان زمین شناسی و اکتشافات معدنی کشور
زبان مرجع: انگلیسی
خروجی: مقاله، داده های الکترونیکی
ناظران علمی: صفیه حقانی
نویسندگان: صفیه حقانی، سوزان آ.جی. لروی، اینگمار بیورن اونکل، ژان لوئیس ریس،
چارلی اس. بریستو، حمید علیزاده لاهیجانی، عبدالمجید نادری بنی، حمید نظری، محمدرضا
انسانی
رئیس کرسی یونسکو در مخاطرات زمین شناختی ساحلی: حمید نظری
مسئول شورای اجرایی: راضیه لک
خلاصه نویسی و ترجمه به انگلیسی: منوچهر قرشی
ناشر: نشر خزه
با همکاری کرسی یونسکو در مخاطرات زمین شناختی ساحلی
چاپ اول: ۱۴۰۳
شمارگان: ۵۰ نسخه
صفحات: ۱۰۴
شابک: ۹۷۸-۶۲۲-۸۴۲۳-۲۲-۷

khazepub@gmail.com



UNESCO Chair on
Coastal Geo-Hazard Analysis
Research Institute for Earth Sciences
Geological Survey of Iran



Report Information

Title: Morphology of the Sefidrud Delta (Southwest Caspian Sea): a tectonically-driven Gilbert delta

Employer: Brunel University London, CEREGE, Technopôle de l'Arbois-Méditerranée, Institute for Ecosystem Research, Kiel University, Laboratory for Climate Sciences and the Environment, Birkbeck University, Iranian National Institute for Oceanography and Atmospheric Science (INIOAS), Research Institute for Earth Sciences, Geological Survey of Iran

Original language: English

Output: Paper, Digital Meta Data

Supervisors: Safiyeh Haghani

Authors: Safiyeh Haghani, Suzanne A.G. Leroy, Ingmar Björn Unkel, Jean Louis Reyss, Charlie S. Bristow, Hamid A.Z. Lahijani, Abdolmajid Naderi Beni, Hamid Nazari, Mohammad Reza Ensani

Chairholder in the UNESCO Chair on Coastal Geo-Hazard Analysis:
Hamid Nazari

Head of the Executive Council: Razyeh Lak

Summarized and translated into English: Manouchehr Ghorashi

Publisher: Khazeh Publication

with cooperation UNESCO Chair on Coastal Geo-Hazard Analysis

First Edition: 2024

Edition number: 50

Page: 104

Shabak: 978-622-8423-22-7

khazepub@gmail.com

| Scientific Council | |
|---------------------------|---|
| Name | Affiliation |
| Behrouz Abtahi | Shahid Beheshti University (SBU) |
| Philippe Agard | University of Sorbonne |
| Justin Ahanhanzo | Intergovernmental Oceanographic Commission of UNESCO (IOC-UNESCO) |
| Hamid Alizadeh Lahijani | Iranian National Institute for Oceanography and Atmospheric Science |
| Ryo Anma | Tokushima University |
| Franck A. Audemard | Department of Geology, Central University of Venezuela |
| Alice Aurelie | UNESCO Water Sciences Division |
| Ara Avagyan | IGS: Institute Geological Sciences |
| Yeong Bae Seong | Korea University |
| Rick J Bailey | IOC-UNESCO Indian Ocean Tsunami Warning and Mitigation System/ UNESCO |
| Abbas Banj Shafiei | Urmia University |
| Eric Barrier | University of Sorbonne |
| Yahya Djamour | Shahid Beheshti University (SBU) |
| Issa El-Hussain | Sultan Qaboos University |
| Aram Fathian Baneh | University of Calgary |
| Hassan Fazeli Nashli | University of Tehran |
| Magdi Guirguis | Institut français d'archéologie orientale du Caire |
| Martin Hanz | German under water archaeology association |

| | |
|---------------------|---|
| Ekkehard Holzbecher | German University of Technology in Oman |
| Egor Krasinskiy | Underwater research center Russian Geographical Society |
| Razyeh Lak | Research Institute for Earth Sciences |
| John Lambert | Deltares, UNESCO |
| Mohammad Mokhtari | International Institute of Earthquake Engineering and Seismology |
| Hamid Nazari | Research Institute for Earth Sciences |
| Jafar Omrani | Geological Survey of Iran |
| Klaus Reicherter | Aachen University |
| Jean-François Ritz | University of Montpellier |
| Stefano Salvi | National Institute of Geophysics and Volcanology (INGV) |
| Morteza Talebian | Research Institute for Earth Sciences |
| Mohammad Tatar | International Institute of Earthquake Engineering and Seismology |
| Judith Thomalsky | German Archaeological Institute Tehran Branch |
| Richard Walker | University of Oxford |
| Wenjiao Xiao | Chinese Academy of Sciences |
| Alireza Zarasvandi | Iranian Research Organization for Science & Technology (IROST) – Ministry of Science, Research & Technology |
| Mahdi Zare | International Institute of Earthquake Engineering and Seismology |

| Executive Committee | |
|----------------------------|---|
| Name | Affiliation |
| Nasir Ahmadi | Environmental Protection Organization of Mazandaran Province |
| Arash Amini | Golestan University |
| Alireza Amrikazemi | Scientific Coordinator, Qeshm Island UNESCO Global Geopark |
| Parviz Armani | Imam Khomeini International University |
| Ataollah Dadashpour | Geological Survey of Iran, Sari branch |
| Asghar Dolati | Kharazmi University |
| Hasan Fazelinashli | University of Tehran |
| Fahimeh Foroghi | Iranian National Institute for Oceanography and Atmospheric Science |
| Abdolazaim Ghanghormeh | Golestan University |
| Habibolah Ghasemi | Shahrood University of Technology |
| Mohammad reza Ghasemi | Research Institute for Earth Sciences |
| Manouchehr Ghorashi | Research Institute for Earth Sciences |
| Ahmed Hadidi | German University of Technology in Oman (GUTECH) |
| Jafar Hassanpour | University of Tehran |
| Ataollah Kavian | Environmental Protection Organization of Mazandaran Province |
| Razyeh Lak | Head of RIES and Executive Manager |
| Mahmoudreza Majidifard | Research Institute for Earth Sciences |
| Majid Moghadam | Iranian Research Organization for Science & |

| | |
|------------------------|---|
| | Technology (IROST) |
| Ali Akbar Momeni | Shahrood University of Technology |
| Babak Moradi | Iranian National Institute for Oceanography and Atmospheric Science |
| Seyed Mohsen Mortazavi | Hormozgan University |
| Hasan Nasrollah Zadeh | Caspian Sea Ecological Research Center |
| Ehsan Pegah | Kharazmi University |
| Abdolwahed Pehpouri | Qeshm Island UNESCO Global Geopark |
| Ahmadreza Rabani | University of Science and Technology of Mazandaran |
| Mahdi Rahmanian | Shargh Daily newspaper |
| Ahmad Rashidi | International Institute of Earthquake Engineering and Seismology |
| Masoud Sadri Nasab | University of Tehran |
| Mohammad Tatar | International Institute of Earthquake Engineering and Seismology |
| Alireza Vaezi | Research Institute for Earth Sciences |
| Mojtaba Yamani | University of Tehran |
| Secretariat | |
| Name | Affiliation |
| Elnaz Aghaali | Research Institute for Earth Sciences |
| Keivan Ajdari | Research Institute for Earth Sciences |
| Hourieh AliBeygi | Research Institute for Earth Sciences |
| Bahman Bahrami | Memaran Asr Ertebat Company |
| Hanieh Bakhshaei | Geological Survey of Iran |

| | |
|------------------------------|---------------------------------------|
| Reza Behbahani | Geological Survey of Iran |
| Javad Darvishi khatooni | Geological Survey of Iran |
| Mohammadreza Ensani | Geological Survey of Iran |
| Marziyeh Estrabi Ashtiyani | Geological Survey of Iran |
| Sedigheh Ghanipour | Research Institute for Earth Sciences |
| Elaheh Ghayoumi | Memaran Asr Ertebat Company |
| Gholamreza Hoseinyar | Geological Survey of Iran |
| Mojtaba Kavianpour Sangno | Geological Survey of Iran |
| Zeinab Kazeminia | Research Institute for Earth Sciences |
| Hamoon Memarian | Research Institute for Earth Sciences |
| Mehrnoosh Pour Saeid | Graphic Designer |
| Shirin Safavi | Research Institute for Earth Sciences |
| Aazam Takhtchin | Research Institute for Earth Sciences |

CONTENTS

| | |
|--|----|
| Abstract | 1 |
| 1- Introduction | 4 |
| 2- Study area | 8 |
| 2-1- <i>Caspian catchment area and river system</i> | 8 |
| 2-2- <i>The Sefidrud and its delta</i> | 10 |
| 3- Materials and methods..... | 12 |
| 3-1- <i>Seismic profiles and sub-aqueous sampling</i> | 12 |
| 3-2- <i>Ground Penetrating Radar (GPR) and sub-aerial sampling</i> | 14 |
| 3-3- <i>Sedimentology and chronology</i> | 16 |
| 3-4- <i>Macro–remains and palynology</i> | 19 |
| 3-5- <i>Geochemical proxies</i> | 20 |
| 4- Results | 22 |
| 4-1- <i>Morphology of the modern delta</i> | 22 |
| 4-2- <i>Structure and sediments of the delta subsurface</i> ... | 24 |
| 4-3- <i>Radionuclide and radiocarbon dating</i> | 32 |
| 4-4- <i>Macro–remains</i> | 35 |
| 4-5- <i>Palynology</i> | 39 |
| 4-6- <i>Geochemical analysis</i> | 47 |
| 4-6-1- <i>Siliciclastic proxies</i> | 47 |
| 4-6-2- <i>Carbonate proxies</i> | 49 |

| | |
|---|----|
| 4-6-3- Iron and manganese | 52 |
| 4-7- <i>Radar profiles and sedimentary facies</i> | 52 |
| 5- Discussion..... | 57 |
| 5-1- <i>A Gilbert-like delta</i> | 57 |
| 5-2- <i>Sedimentation rate and sediment delivery to the basin</i> | 59 |
| 5-3- <i>Indicators of water level changes</i> | 62 |
| 6- Conclusions | 69 |
| Appendix A. Core photos (photo by S. Haghani). The number in bracket is water depth. | 72 |
| Appendix B | 73 |
| Reference: | 75 |

Table of Figures

| | |
|--|----|
| Figure 1: Caspian Sea level; 900 to 1900 from Naderi Beni et al., (2013); 1900 to 1992 from Lepeshevkov et al., (1981); 1992 to 2016 from USDA (2017). | 6 |
| Figure 2: A: Location map of the Caspian Sea (white lines represent international boundaries.) and major rivers flowing to the Caspian Sea. Mt.: Mountains, B: Google Earth image of the study area showing the lowland located between Alborz Mountains and the Caspian Sea, C: Location of the cores, surface samples, seismic and GPR profiles taken from Sefidrud delta, red dashed line represents submarine delta limit from Kazancı and Gulbabazadeh (2013), D: GPR profile 114, E: GPR profiles 123 and 125, F: GPR profiles 104 and 105, G: GPR profiles 106 and 107..... | 18 |
| Figure 3: Topographic profiles of the sub-aqueous part of Sefidrud Delta based on seismic profiles. For the location of seismic profiles, see Figure 2 B. | 23 |
| Figure 4- Internal structures in seismic profile 35 displaying horizontal, crossbedding and clinoform reflectors. The red line in B indicates the basal unconformity..... | 27 |
| Figure 5- Digital Elevation Model of the Sefidrud Delta in the study area. Red lines: seismic profiles, black stars: Core locations | 29 |
| Figure 6- Sedimentary log for the marine sequence, displaying core photo and water depth in parentheses below the name of the core, sedimentary facies, grain size (clay, silt and sand), magnetic susceptibility (MS), organic matter (OM) and calcium carbonate (CaCO ₃). The black star refers to the depth of the radiocarbon date..... | 31 |
| Figure 7- Distribution of silt, sandy silt and silty sand in surface samples from offshore. | 32 |

Figure 8- Radionuclide dating of core NSM14G3, based on CRS (constant rate of supply) model. (A): Profiles of ^{210}Pb activities (Bq kg^{-1} , dry weight) with depth in cm. The regression line corresponds to an average sedimentation rate of 1.67 mm/yr. (B): Profiles of ^{137}Cs activities (fallout from nuclear weapon testing) with depth in cm. (C): Radionuclide dating of core NSM14G3, based on constant sedimentation rate, Profiles of ^{210}Pb activities (Bq kg^{-1} , dry weight) with depth in cm..... 35

Figure 9- Macro-remains above $125\mu\text{m}$ of the five short offshore cores in percentages and concentration. The black dots represent very low percentages and concentration of macro-remains. The black star refers to the depth of the radiocarbon date..... 39

Figure 10- A: Surface samples, B: Pollen, spores, non-pollen palynomorphs and dinocyst diagram for the core NSM14G3. Black dot for values $<0.5\%$. The numbers below the core names represent water depth..... 46

Figure 11- Pearson correlation matrix of elemental pairs on NSM14G5 sequence, blue colours and the rising line pattern indicate a positive correlation whereas red colours and the descending line pattern indicate negative values. The strength of correlation or anticorrelation increases with colour shades. 48

Figure 12- Environmental proxies from core NSM14G5: Mn/Fe ratio as indicator for oxic vs. anoxic; Ca/Sr ratio as indicator for detrital vs. biogenic carbonate input; Cl content as indicator of marine environment; Zr/Rb ratio as an indicator for grain size distribution; Si content. The black star refers to the depth of radiocarbon date..... 51

Figure 13- Ground Penetrating Radar (GPR) profiles from Sefidrud delta, for the location of the profiles see Fig. 2.

Purple lines represent the main reflectors for interpretation. See appendix B for core descriptions. 56

Figure 14- Palynology and Macro-remains from the NSM14G3 against Caspian Sea Level, the data from 1100 to 1900 from Naderi Beni et al. (2013); 1900 to 1992 from Lepeshevkov et al. (1981); 1992 to 2016 from USDA (2017). Orange and blue ribbons represent periods of low-stands and high-stands, respectively. 64

Figure 15- Geochemical and Macro-remains plot, from NSM14G5 against Caspian Sea Level, for the Caspian Sea Level during last millennium: the data from 1100 to 1900 from Naderi Beni et al. (2013); 1900 to 1992 from Lepeshevkov et al. (1981); 1992 to 2016 from USDA (2017). Orange and blue ribbons represent periods of low-stands and high-stands, respectively. The Caspian Sea Level during last millennia from Kroonenberg et al. (2008). 68

Figure 16: Appendix A 72

Figure 17: Appendix B: Sedimentary log for cores taken on GPR profiles, displaying sedimentary facies, sedimentary zone, core photo, grain size (clay, silt and sand) and magnetic susceptibility (MS). The black pin symbols show the core section limits. Black stars show the location of the dated samples. 74

Table of Table

| | |
|---|----|
| Table 1: Length and location of offshore cores | 13 |
| Table 2: Location of surface samples offshore | 14 |
| Table 3: Radiocarbon ages from core NSM14G5 and Kiashahr palaeo beach, calibrated using CALIB | 19 |
| Table 4-Sedimentation rates in the southern Caspian Sea. See figure 2A and 2E for the location of the cores programme version 7.1, with the Marine13 calibration curve (Reimer et al., 2013). | 33 |

Abstract

This manuscript presents the internal facies architecture of the sediment in the upper layers of the Sefidrud delta, located along the south Caspian Sea coast. The delta lies between the subsiding southern basin and the uplifting Alborz Mountains, with its sharp topography shaped by several faults. It features a fine-grained, large Gilbert-type delta, primarily significant for paleoenvironmental studies and oil exploration. However, publications on the offshore sediments of the South Caspian Basin are scarce. This study examines both offshore and nearshore/onshore areas, employing sedimentology, palynology, macro-remains, geochemistry, and radar profiles to refine previous reconstructions. The delta extends at least 70 km SW-NE, characterized by a flat delta plain facing a steep delta front with a 60° inclined ramp surface, leading to a 20° prodelta. An incised valley was noted, limited to the delta front and influenced by the steep slope. Sedimentation rates are under 2 mm yr⁻¹: 1.9 mm yr⁻¹ for the delta plain, 1.8-1.2 mm yr⁻¹ for the delta front, and 0.39 mm yr⁻¹ for the prodelta. The basin is tide-free, with waves playing a minimal role in offshore deposition. The modern Sefidrud delta serves as an analogue for predictive stratigraphical and sedimentological models of steep ancient deltas affected by rapid base-level changes and transversal faults. This study enhances the understanding of facies distribution and three-dimensional geometry in fine-grained, high-gradient Gilbert-type deltas. The analysis reveals various sedimentary structures indicative of dynamic

depositional environments. The upper delta plain presents complex interleaving of fluvial and tidal deposits, where sedimentation is largely dominated by riverine processes and influenced by episodic flooding events. This interplay is evident in the sedimentary facies that transition from sand-rich, channel-fill deposits to finer, more overbank sediments. Palynological data further support the interpretation of a variable paleoenvironment, suggesting alternating periods of marine and freshwater influence consistent with base-level fluctuations. In contrast, the steep delta front exhibits distinctive features, such as cliffed embankments and avalanche deposits, which signify rapid sediment delivery from the deltaic system. The high-angle accumulations demonstrate the energetic conditions that govern deposition in such high-gradient settings, where sediment bypass is promoted by the steep slope. The identified sediments, characterized by significant clay fractions, indicate a high degree of texture sorting influenced by gravitational processes rather than wave action. Geochemical analyses point to variations in organic content across the delta, suggesting differing depositional environments. Increased organic richness in the prodelta sediments aligns with the accumulation of fine-grained material, particularly in areas where stagnation allows for preservation of organic matter. This information is crucial for understanding potential hydrocarbon reservoirs in the region, as it highlights zones conducive to organic matter kerogen maturation. Moreover, the radar profiles collected along the delta's stratigraphic columns offer insight into the subsurface architecture, revealing stacked depositional

units that reflect the complex facies interactions over time. This multi-faceted approach not only refines the existing geological models of the Sefidrud delta but also serves as an essential reference for analogous coastal sedimentary systems worldwide. As further studies delineate the subsurface configurations and depositional dynamics, it is anticipated that this research will directly contribute to improved resource management and ecological conservation efforts in the South Caspian Basin.

Keywords: River delta, sedimentation rate, South Caspian Basin, Gilbert delta, seismic profile, geochemistry, palynology.

1- Introduction

The Sefidrud Delta, located southwest of the Caspian Sea between the sinking south basin and the rising Alborz Mountains, is classified as a fluvial-wave interaction delta (Reading, 2009), with sediments redistributed by eastward longshore currents. Uplifting along the Khazar Fault ranges from approximately 5 mm/yr in the northeast to about 2 mm/yr in the northwest (Djamour et al., 2010). The south Caspian Basin has been rapidly subsiding for at least the last 5 million years (Brunet et al., 2003). Wave-influenced deltas can exhibit symmetric or asymmetric morphodynamics depending on the balance between river flow and wave energy (Preoteasa et al., 2016; Fig. 3 in Haghani et al., 2016b). In addition to waves and currents, rapid water level fluctuations significantly impact the delta's formation and development. The Sefidrud Delta, without tidal influence, exemplifies the contributions of river and wave activity in shaping its lobes (Kazancı et al., 2013; Fig. 3 in Haghani et al., 2016b). Understanding the morphology and geometry of deltas is crucial for the petroleum industry, as they often serve as excellent oil and gas reservoirs (Selly, 1996). However, studies on the geometry of the Sefidrud Delta remain limited. Its morphology is shaped by factors such as shelf gradient, wave energy, longshore currents, and sediment supply influenced by fluctuating Caspian Sea levels.

The Caspian Sea has experienced a ten-meter rise and fall during the Medieval Climate Anomaly (MCA) and Little Ice Age (LIA), significantly exceeding oceanic

rates (Figure 1). The submarine portion of the Sefidrud Delta represents a major, yet unexplored, archive for studying sea level fluctuations. High sedimentation rates on steep adjacent slopes provide a valuable geological record of Caspian Sea level changes over the past millennium, such as the deep-sea sequences in the south basin (Leroy et al., 2013b). Nevertheless, no offshore investigations of the Sefidrud Delta have been published, with key studies primarily conducted by Kazancı and Gulbabazadeh (2013), Naderi Beni et al., (2013b), and Lahijani et al., (2009).

Morphology of the Sefidrud Delta (Southwest Caspian Sea): a tectonically-driven Gilbert delta

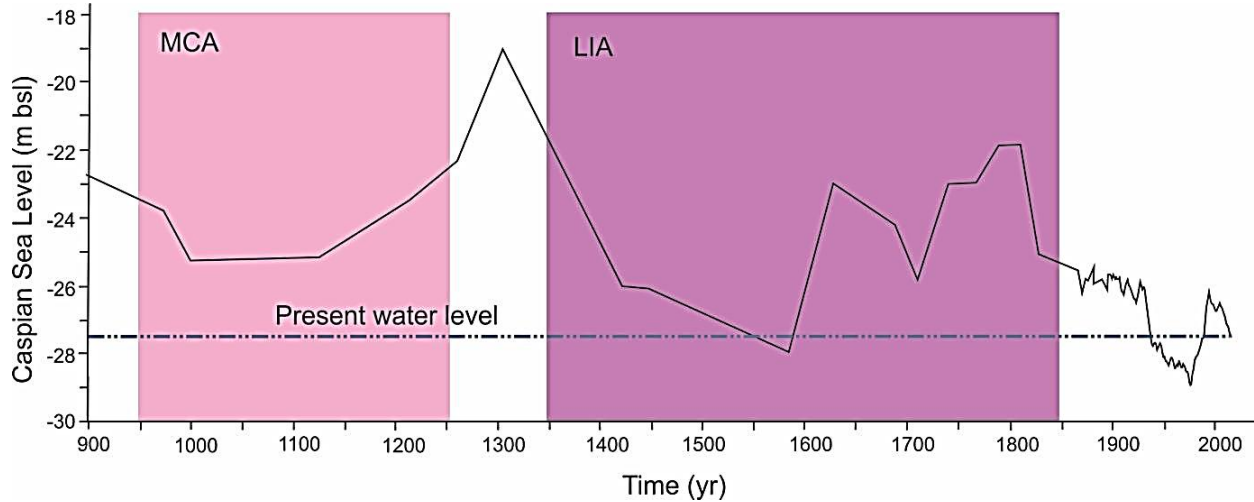


Figure 1: Caspian Sea level; 900 to 1900 from Naderi Beni et al., (2013); 1900 to 1992 from Lepshevkov et al., (1981); 1992 to 2016 from USDA (2017).

Kazancı and Gulbabazadeh (2013) focused on the initiation of the modern delta probably formed during the last three millennia and two older stages of the delta evolution in Late Khvalynian and Early Khvalynian. Their work is based on onshore field work samples and data gathering and it is the first publication on the evolution of the Sefidrud Delta. However, no age data were included. The authors proposed a concept of lobe evolution, partially based on a conceptual model.

Naderi Beni et al., (2013) studied Kiashahr, Boujagh and Amirkola Lagoons using Ground Penetrating Radar (GPR) profiles supported by several radiocarbon age estimates on Kiashahr spit. They concluded that the development of these lagoons was a response to rapid CSL rise during the LIA. The results from the present study will show time hiatuses that complicate the evolutionary model of these authors.

Lahijani et al., (2009) studied the coastal evolution of the Sefidrud Delta including lagoon development in the area. The authors suggested that the Zibakenar and Kiashahr Lagoons developed during the past four centuries, yet new age data were not included.

The main aim of this study is to provide an overview of geometry, structure, and facies of the Sefidrud Delta, combining the offshore, onshore, and inland environments. The present research concentrates on (1) the morphology and sedimentology of aerial and subaqueous delta, (2) the structure of the delta

subsurface, investigated by acoustic profiling (ground penetrating radar and seismic profiles) and coring (87 to 486 cm long cores), and (3) sedimentation rate in different parts of the delta. This study is the first in-depth study of the Sefidrud delta that combines the offshore, onshore and inland environments. This study also attempts to record Caspian Sea level fluctuations using high-resolution analyses (macrofossils, palynological and geochemical analyses) of a well-dated sequence (conventional ^{14}C and radionuclide dating).

2- Study area

2-1- Caspian catchment area and river system

With a 3.5 million km² catchments area (~10 times larger than its surface area), the Caspian Sea is the largest lake on Earth, mainly located in littoral states of Iran, Turkmenistan, Kazakhstan, Russia and Azerbaijan, and small parts in Turkey, Armenia and Georgia (UNEP, 2006) (Figure 2A). The northern part of the basin is located in high latitude forests, middle Volga steppe and Pre-Caspian deserts. The western and southern parts of the basin are situated in high mountains of Caucasus and Alborz, respectively. The southern part is extremely faulted and the Khazar, Lahijan, Astara and Rudbar faults are the main faults in the area (Figure 2A). The Kopet-Daq Mountains cover the south-eastern part and the eastern part is dominated by wide area of deserts. The salinity in the Caspian Sea increases from the north

to the south. In the south and middle basin, it is brackish around 13 psu; while it is nearly fresh in the northern basin (0.1 psu), especially near to Volga River (Kostianoy and Kosarev 2005). Among more than 130 rivers that flow into the CS, five rivers form significant deltas. In the north, the Volga and Ural Rivers as the main water supplier of the CS have formed very large deltas, now both with a significant emerged part. The areas of the Volga and Ural Rivers are shallow water. The delta of Terek (north-west coast) begins 170 km away from the sea and its network is complicated by numerous branches, lakes and artificial channels (Figure 2A). Within the Terek delta, two waterworks facilities were constructed which redistributed the runoff between the mainstream of the delta and the irrigation channels in its northern part. The river flows into the southwestern coastal area on North Caspian Basin, where the water depth is less than 5 m. The fourth largest delta of the CS, Kura delta, represents the Kura-Araks lowlands. The construction of Mingechaur Reservoir in the 1950s has significantly reduced the volume of the sediments delivered to the basin by more than 50%. In the present-day delta, dry channels and dried lagoons are recognised (Kosarev and Kostianoy, 2005). The sea area offshore the Kura River delta is rather deep. On the southern coast of the Caspian Sea, the 820 km-long Sefidrud River as the main sediment supplier to the CS has formed a large delta.

2-2- The Sefidrud and its delta

The Sefidrud, the fifth river to form a significant Caspian delta and the second longest river of Iran, originates in the Zagros Mountains, and is fed by a great number of tributaries, penetrates the Alborz Mountains and flows into the Caspian Sea. Before cutting the Alborz Mountains, the Sefidrud is named the Kizilozen, also spelled as Qezel-Uzen, (the Red River) which is a Tatar name, and after capturing the Shahrud (the King River) it is known as the Sefidrud which is Persian name signifies “the white river” (Figure 2A). The area between the foot of the Alborz Mountains where the apex of the delta is located and the Caspian Sea, close to the break between the delta plain and the delta front, is known as coastal lowlands and has a very flat topography (Figure 2B).

The deposition setting imposes a set of conditions on a sedimentary system that will lead to a predictable stratigraphic response in other locations under similar conditions, assuming similar internal behaviour. For the Sefidrud delta, the sedimentary system conditions are as follows:

Sefidrud water discharge is 4 km³/year and the sediment discharge is 32 million tons/year (Lahijani et al., 2008).

The catchment area is large and steep, with a circa 67,000 km² drainage area.

The receiving basin has a high gradient seafloor, flanked by the steep mountains of the Alborz, Caucasus and Kopet-Daq. From another point of view, the receiving basin can also be divided to two parts: aerial and aqueous. The aerial break refers to the aerial slope break at the foot of the Alborz Mountains (Figure 2B), while the aqueous break refers to the slope break between delta plain and delta front.

Winds are strong from north and northwest directions. The meridional wind stress (in the winter directed southward) plays an important role in generating an eastward longshore current.

Waves are smaller in summer than in winter. Wave and wave-induced currents are the main factors in delta configuration (Krasnozhan, et al., 1999; Lahijani et al., 2008; Haghani and Leroy, 2016; Haghani et al., 2016b).

Agriculture is the dominant land-use within the aerial part of the Sefidrud delta.

Since the CS is tide free, none of its deltas are tidally influenced and deltaic outbuilding typically involves shoreline progradation.

The Sefidrud diverted its course in the last centuries by 23 km from the east, near Amirkola Lagoon, towards the west near Kiashahr (Krasnozhan et al., 1999; Lahijani et al., 2009; Leroy et al., 2011; Kazancı and

Gulbabazadeh, 2013; Naderi Beni et al., 2013; Haghani and Leroy, under review). It is known as the Old Sefidrud before avulsion and Sefidrud (or New Sefidrud) thereafter (Figure 2C). Before the avulsion, Kiashahr was a linear coastline that at present remains as a ‘palaeo-beach’ (Kousari, 1986) (Figure 2C). After the avulsion happened, the Sefidrud constructed a new small triangle-shaped delta prograding into the Caspian Sea (Haghani et al., 2016b) and the linear coastline was replaced by an arcuate coastline.

3- Materials and methods

3-1- Seismic profiles and sub-aqueous sampling

Seven seismic profiles were acquired from the offshore area using the Parametric Echosounder System (SES 2000) from Innomar (Wunderlich and Müller, 2003), which provides high and variable low (4–12 kHz) frequency signals at water depths of 0.5 to 800 m with a vertical resolution of less than 5 cm. All the profiles were collected perpendicular to the coastline (Figure 2C). SESWIN data acquisition software was used to collect the data. The echosounder data were subsequently edited using the post-processing software ISE from Innomar. The maximum length of the profiles reached up to 24 km in profile 30 with the maximum penetration depth of circa 25 m. The objective of using

seismic profiles was to make a 3D morphology of subaqueous Sefidrud delta and especially to characterise its steep nature.

Five cores with a maximum length of 157 cm were retrieved using a gravity corer from the CS at the water depths of 17, 105, 301, 431 and 470 m (Figure 2C, Table 1). The cores were taken in front of the current main distributary of the Sefidrud. Furthermore, surface samples were taken using a grab sampler in order to document the modern plume of the main distributary (Figure 2C). The water depths varied between 15 to 20 m (Table 2).

Table 1: Length and location of offshore cores

| Core Number | Location | | Water depth (m) | Distance from the coast (km) | length (cm) |
|-------------|---------------|----------------|-----------------|------------------------------|-------------|
| | Longitude | Latitude | | | |
| NSM14G1 | 37°29'59.87"N | 49°54'15.79"E | 17 | 3 | 145 |
| NSM14G2 | 37°32'47.82"N | 49°54'6.07"E | 105 | 8.2 | 157 |
| NSM14G3 | 37°33'59.53"N | 49°53'41.831"E | 301 | 10.5 | 150 |
| NSM14G4 | 37°34'46.36"N | 49°53'29.23"E | 431 | 12 | 87 |
| NSM14G5 | 37°35'19.06"N | 49°53'18.474"E | 470 | 13 | 113 |

Table 2: Location of surface samples offshore

| Sample ID | Location | | Water depth (m) |
|-----------|---------------|----------------|--------------------|
| | Longitude | Latitude | |
| M14GB1 | 37°30'07.50"N | 49°56'57.24"E | 16 |
| M14GB2 | 37°29'42.50"N | 49°58'26.80"E | 18.9 |
| M14GB3 | 37°29'15.00"N | 49°59'39.8"E | 19 |
| M14GB4 | 37°28'30.80"N | 50°00'41.00"E | 16 |
| M14GB5 | 37°27'47.00"N | 50° 01'18.58"E | 15 |
| M14GB6 | 37°27'14.01"N | 50° 2'07.77"E | 15 |
| M14GB7 | 37°27'04.90"N | 50° 3'41.81"E | 19.5 |
| M14GB8 | 37°26'35.00"N | 50° 5'35.48"E | 18 |
| M14GB9 | 37°26'15.40"N | 50° 7'43.49"E | 18.2 |
| M14GB10 | 37°25'22.33"N | 50° 9'49.80"E | 18 |
| M14GB11 | 37°24'59.71"N | 50° 11'03.11"E | 17 |
| M14GB12 | 37°24'42.72"N | 50°12'17.90"E | 17 |
| M14GB13 | 37°24'30.50"N | 50°13'57.65"E | 20 |
| M14GB14 | 37°23'03.08"N | 50°16'22.90"E | 20.1 |
| M14GB15 | 37°22'02.90"N | 50°17'02.81"E | 19.5 |

3-2- Ground Penetrating Radar (GPR) and sub-aerial sampling

Seven GPR profiles were taken in four onshore locations (i.e. Figure 2D to Figure 2G), using a RAMAC/GPR system. The antenna separation distance was fixed at 1 m to obtain the antenna frequency of 100

MHz. This frequency should allow a good penetration depth (10-20 m) in an ideal condition (e.g. low water table and low salinity). In order to interpret depositional environments and to link the GPR results with sedimentological data, one core was collected along each radar profile (Figure 2D to Figure 2G), using a percussion corer. Sedimentological analyses including magnetic susceptibility, grain size, organic matter and carbonate content were performed on the cores. The software Reflex W 2D/3D was used for processing the data. Different standard processing such as subtract DC shift, automatic static correction, gain function, band pass filtering and running average filter were used to provide a more realistic subsurface image. The lack of topographic mapping was a weak point of processing data. However, all the profiles were taken from flat or relatively flat surfaces with a dip of less than 10° . Lengths of the profiles vary between 290 and 920 m, with the maximum penetration depth of 4 m. The objective of the GPR in this study was to image the internal structure of sediments in order to identify the mechanism of delta building. Another objective was to identify any hidden/buried lagoon in the study area.

Except for GPR profiles 106 and 107, all other profiles were taken from saturated sand sediments. Vertical resolution of the profiles is considered to be one-quarter of the wave-length of the radar signal in the grounds (Reynolds, 1977). Wavelength is a function of both antenna frequency and the velocity of the radar

signal through the ground (Bristow, 2009). The velocity of the radar signal for saturated sand is 0.06 m/ns. A 100 MHz transmitter has a pulse period of 10 ns and in saturated sand where velocity is 0.06 m/ns, the wavelength will be 0.6 m and the resolution will be one quarter on the wavelength or 0.15 m (i.e. $0.6 \text{ m} \times 0.25 = 0.15 \text{ m}$). GPR profiles 106 and 107 were taken from silt sediments. The velocity of radar signal for saturated silt is 0.07 m/ns and therefore the resolution will be 0.175 m (i.e. $0.7 \text{ m} \times 0.25 = 0.175 \text{ m}$). Vertical resolution has important implications for its sedimentological interpretation, because it will determine the scale of sedimentary structure that can be observed (Neal, 2004; Bristow, 2009). Therefore, in this study, the strata with a minimum thickness of 15 cm in sand and 17.5 cm in silt will be recognisable in the GPR profiles.

3-3- Sedimentology and chronology

Magnetic susceptibility (MS) measurements were performed on all the cores using a Bartington MS2C core logging sensor at 2 cm intervals. A standard visual core description was performed immediately after core photography (Mazzullo et al., 1988) and sediment colour was determined using a Munsell Colour Chart. Grain size analyses were performed on homogenised and representative subsamples, using a CILAS 1180 particle size analyser. Granulometric data were processed using the GRADISTAT program (Blott and Pye, 2001) and the sand-silt-clay triangular diagram proposed by Folk

(1974) was used for naming the textural group of the sediments. Organic matter (OM) and calcium carbonate (CaCO₃) were determined through loss on ignition (LOI) (Heiri et al., 2001).

Radionuclide analyses were measured on core NSM14G3, using a very low-background, high-efficiency well-type detector at the laboratory of Modane in the French Alps. ²¹⁰Pb and ¹³⁷Cs records were obtained and ²¹⁰Pb values reach nearly to a back ground at 24 cm depth. Furthermore, a radiocarbon date was obtained from the base of core NSM14G5 at 111 cm depth at 14Chrono Centre, Queen's University Belfast. In sub-aerial part of delta (core 104, in Figure 2F), two radiocarbon dates were obtained from two bivalve shells (*Cerastoderma glaucum*) at Australian Nuclear Science and Technology Organisation (ANSTO). Three radiocarbon ages were then calibrated using the CALIB programme version 7.1 (Stuiver and Reimer, 1993) with the Marine13 calibration curve (Reimer et al., 2013) (Table 3).

Morphology of the Sefidrud Delta (Southwest Caspian Sea): a tectonically-driven Gilbert delta

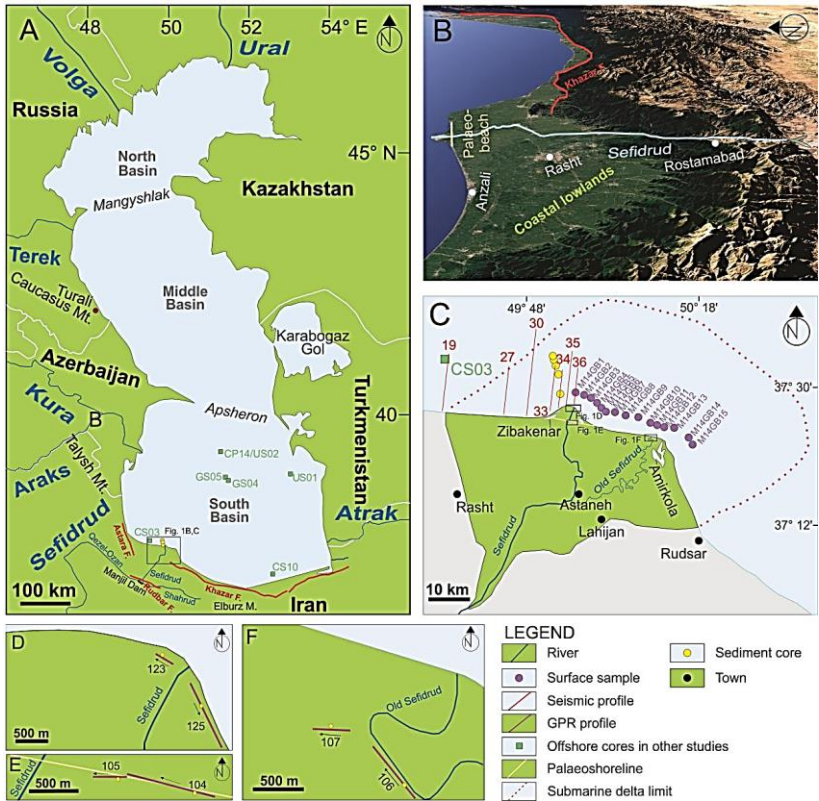


Figure 2: A: Location map of the Caspian Sea (white lines represent international boundaries.) and major rivers flowing to the Caspian Sea. Mt.: Mountains, B: Google Earth image of the study area showing the lowland located between Alborz Mountains and the Caspian Sea, C: Location of the cores, surface samples, seismic and GPR profiles taken from Sefidrud delta, red dashed line represents submarine delta limit from Kazancı and Gulbabazadeh (2013), D: GPR profile 114, E: GPR profiles 123 and 125, F: GPR profiles 104 and 105, G: GPR profiles 106 and 107.

Table 3: Radiocarbon ages from core NSM14G5 and Kiashahr palaeo beach, calibrated using CALIB

| Laboratory number | Sample ID and location | Depth (cm) | Material Type | ¹⁴ C Age (yr BP) | Calibrated (2σ range) | Median Probability |
|-------------------|------------------------|------------|-----------------------------|-----------------------------|--|--------------------|
| UBA-32547 | NSM5-192, NSM14G5 | 111 | Sediment (bulk) | 2945±44 | 690- 885 BC (98.7%) 682-664 BC (1.3%) | 777 BC |
| OZR390 | KL11V1A 2-54, Kiashahr | 150 | Shell (<i>C. glaucum</i>) | 1190±25 | AD 1161-1284 (100%) | AD 1224 |
| OZR391 | KL11V1A 3-40, Kiashahr | 234 | Shell (<i>C. glaucum</i>) | 380±25 | 0 | - |

3-4- Macro-remains and palynology

Following Birks (2001), eight samples from the NSM14G3 and nine samples from NSM14G5 were selected to survey the vertical changes in macro-remains. Furthermore, in order to investigate the horizontal changes in the macro-remains with the distance from the coast line to the deeper part and to highlight possible mass-wasting transport, three samples were selected in each of the following sequence, i.e. NSM14G1, NSM14G2, and NSM14G4. The samples were scanned in three following fractions: 500, 125 and 53 μm and changes in macro-remains are described based on the percentages in the 125 μm fraction.

Surface samples made of two grab samples (M14 series, Table 2) and five core tops (NSM14 series; Table 1) were analysed. Additionally, eleven samples from the

NSM14G3 core with a volume of 0.5 to 4 ml were taken for palynological analyses. The samples were soaked in 10% tetra-sodium pyrophosphate solution for deflocculation. The samples were then treated with cold HCl (first at 10% and then pure), cold HF (32%), followed by a repeated cold HCl treatment, in order to eliminate carbonates, quartz and fluorosilicate gels, respectively. Finally, the samples were sieved through 125 and 10 μm nylon meshes. The residues were mounted on slides in glycerol. The initial addition of Lycopodium tablets allowed the estimation of concentrations (number of palynomorphs per ml of wet sediment). The median for the terrestrial pollen grains and the dinocysts (excluding varia) were 327 and 153, respectively. The P/D ratio refers to the ratio of the absolute abundance of pollen (P) over dinocysts (D) (McCarthy and Mudie 1998). Pollen identification was made with the Brunel University reference collection and the atlas of Reille (1992, 1995, 1998) and a microscope with a routine magnification of 400x, and the possibility to move to 1000x for more difficult cases. The taxonomy and the ecological preferences of the CS dinocysts are detailed in Marret et al., (2004) and Leroy et al., (2013b).

3-5- Geochemical proxies

Sediment sections from the NSM14G5 core were extracted by using PVC u-channels with 2 cm width and 1 cm depth, and a maximum of 50 cm length. At the Institute for Geosciences, Kiel University (Germany),

the core segments were scanned at 3 mm resolution for selected elements with an Avaatech X-Ray Fluorescence core scanner equipped with a Rhodium tube (Richter et al., 2006). For elements with lower atomic number (Al, Si, P, S, Cl, K, Ca, Ti, Mn, Fe) a scanner setting of 10 kV and 750 μ A was applied, with an exposure time of 20 second. For elements with higher atomic number (Br, Rb, Sr, Zr) a setting of 30 kV and 2000 μ A with an exposure time of 40 second was applied. The XRF measurements at each point represent element intensities in counts per second (cps) which mainly depend on element concentration, but also is affected by matrix effects (Röhl and Abrams, 2000), or by dilution of elements outside the measuring range of the spectrometer (closed-sum effect) (Löwemark et al., 2011). The XRF results were reported as element ratios that can be interpreted as changes in relative concentration of an elemental pair to avoid statistical analysis of data sensitive to the closed-sum effect and elemental ratios being asymmetric (Weltje and Tjallingii, 2008). The elements were also normalized against total counts (tcps) (Cuven et al., 2011). All XRF element plots against depth were shown on a log-scale to enhance visibility of changes and to facilitate graphical comparability between different proxy curves. Analysis and plotting were performed using the software R version 3.2.2 (R Core Team, 2014), where the natural logarithm is used by default. Assessing XRF scan data in a palaeo-environmental and -climatic context is still a semi-quantitative method, as we deal with relative

changes of one element against another, rather than with absolute changes in element concentration. Relationships between different elemental ratios obtained from core NSM5 were explored calculating Spearman's rank coefficients and were presented as a correlation matrix using the corrgram package in R (R Core Team, 2014; Wright, 2014). A strong positive correlation between chemical elements implies a mutual origin controlled by the same process.

4- Results

4-1- Morphology of the modern delta

In order to have an idea of the slope degree in the Sefidrud Delta, the seismic profiles are simplified and the topographic profiles of the sub-aqueous part of the delta are presented in Figure 3. The internal structure of the longest profile, number 35, is presented in Figure 4. Figure 5 presents a 3D bathymetric model of the slope setting of Sefidrud delta based on the water depth data driven from seven seismic profiles using the surfer software, version 13 (Figure 2C and Figure 3).

Morphology of the Sefidrud Delta (Southwest Caspian Sea): a tectonically-driven Gilbert delta

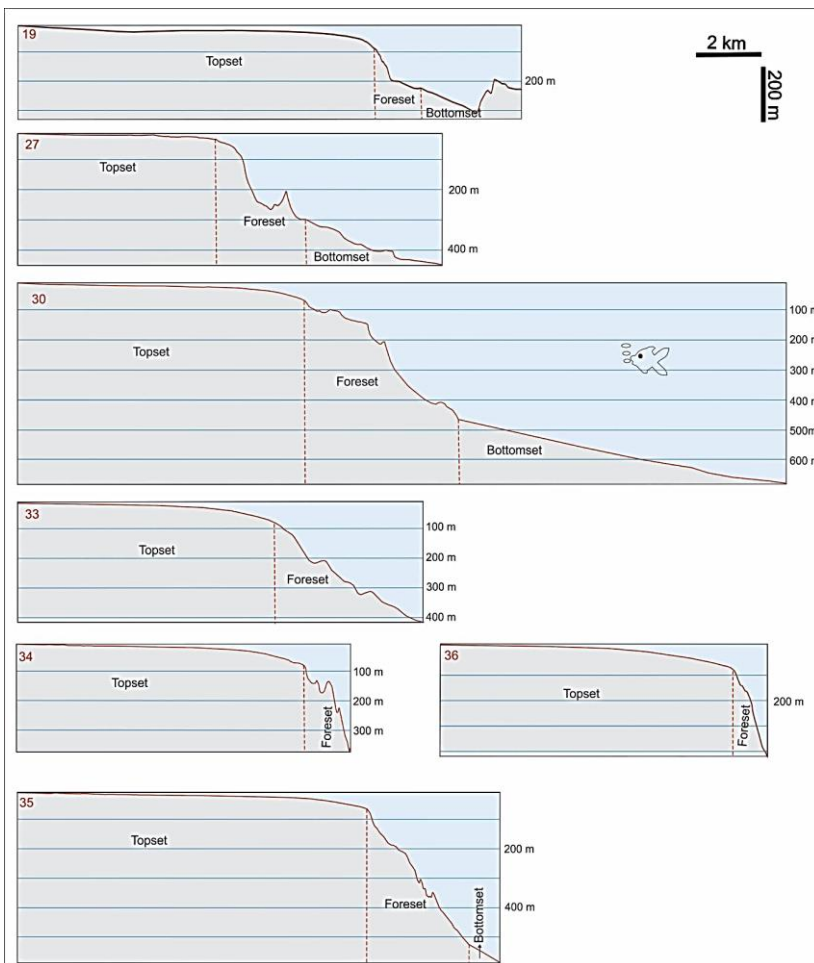


Figure 3: Topographic profiles of the sub-aqueous part of Sefidrud Delta based on seismic profiles. For the location of seismic profiles, see Figure 2 B.

The modern delta is enveloped by sub-aerial and sub-aqueous delta plain, a steep delta front, which passes distally into a gently sloping prodelta area lying around 500 m of water depth (Figure 3 & Figure 5). The slope is very steep near the main river channel (profiles 36 to 34 in Figure 5) and has a low gradient towards the east of the Sefidrud (profiles 33 and 30 in Figure 5) and becomes flat towards Anzali (profiles 27 and 19 in Figure 5). The boundary between delta plain and delta front, the delta rim, is sharp, especially in profiles 34, 35, and 36 (Figure 3) which are located near to the main river channel (Figure 2C).

Based on morphogenetic criteria, the delta plain can be divided to two zones including a fluviially-dominated zone which comprises distributary channels, lagoons, bars and sand spit, and a wave dominated zone which reaches around 90 m in water depth (Figure 3). The delta front areas occupies rather a narrow area trough beyond the delta plain at depths circa 100 m. Subsequently, prodelta appears in the water depth of c. 500 m in front of the Sefidrud mouth

4-2- Structure and sediments of the delta subsurface

A tripartite structure of the Sefidrud Delta was observed in the profiles comprising delta plain, delta front and prodelta containing topset, foreset, and bottomset beds. Profiles 33, 34 and 36 were not long enough to show the bottomset beds. These three components are described in the next section, which

correspond to delta plain, delta front and prodelta, in terms of setting, respectively.

Topsets

The horizontal and crossbedding reflectors (A and B in Figure 4), which are around 7 and 12 m, respectively, represent the topset facies. Topset beds observed in around 9 to 10 km, proximal-to-distal (Figure 3) form around 19 m thick unit of silt, overlaying with the foreset beds. The stratigraphic position and the parallel character of these reflectors imply vertical aggradation in a subaqueous delta plain depositional setting, where the gradient is up to 8°. The unconformity lies at the base of horizontal reflectors, at a depth of 7 m of the sediments, separating this part from the crossbedding part. The thickness of horizontal layers can be attributed to the past seven centuries assuming a 10 mm yr⁻¹ sedimentation rate based on previous dating (Vahabi Moghadam et al., 2007; Sharmad et al., 2012). Core NMS14G1 retrieved from topset beds consist of dark grey to dark greyish brown silt, and contains two layers of shell fragment and bivalve shells. Topset beds show layered clays, with crossbedding sedimentation at 80 to 60 cm (Figure 16 A1, Appendix A), which is in agreement with crossbedding reflectors in seismic profiles (Figure 4). Grain-size analyses performed on surface samples taken from topset beds in the eastern part of the Sefidrud, between New Sefidrud and Old

Sefidrud, show a variation from silt to sandy silt and silty sand (Figure 7). Silty sand only appears in the east (in front of the Old Sefidrud); however, silt and sandy silt are dominant towards the west (Figure 7). Core NSM14G1 at 17 m water depth is silty and this fits well with the westernmost grab samples that are also silty.

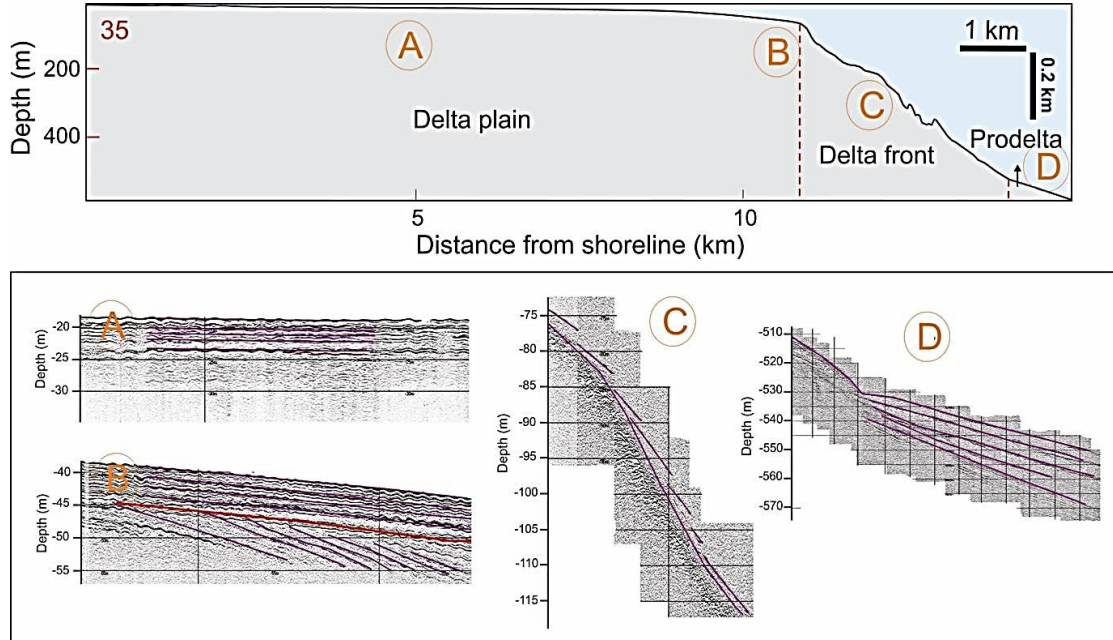


Figure 4- Internal structures in seismic profile 35 displaying horizontal, crossbedding and clinoform reflectors. The red line in B indicates the basal unconformity.

Foresets

After an abrupt change in slope, sigmoid clinoforms are observed in delta front deposits with a gradient of 60° . At this stage, the slope is too steep for significant sediment accumulation and often acts as a by-pass margin. Fine-grain sediments tend to be unstable on the slope and slumping of the sediments may occur which results in re-deposition in deeper parts of the basin. The vertically-oriented structure of the clinoforms (C in Figure 4) may mark the by-pass nature of this part of the basin and represent the delta front. The concave-upward structures in profiles 33 and 34 are suggestive of location of a submerged Sefidrud canyon-channel or less likely a small graben formed between two parallel faults (Figure 5). Foreset beds (e.g. core NSM14G2, G3, and G4) are mainly dominated by dark grey and dark greyish brown silt. The proximal sediments of the foreset beds (e.g. NSM14G2) were marked by dark laminations, which quickly disappear under oxidising condition. These dark laminations were observed also in other offshore sequences of the CS (Leroy et al., 2013a). Bioturbation was observed in core NSM14G3 and the most distal core in foreset beds (e.g. NSM14G4) contains sandy silt layers with sharp contact at 77 cm depth (Figure 6). The foreset beds (NSM14G2, G3, and G4) revealed high gradient crossbedding confirming the observation of the seismic data (e.g. vertically-oriented structure of the clinoforms observed in seismic profiles).

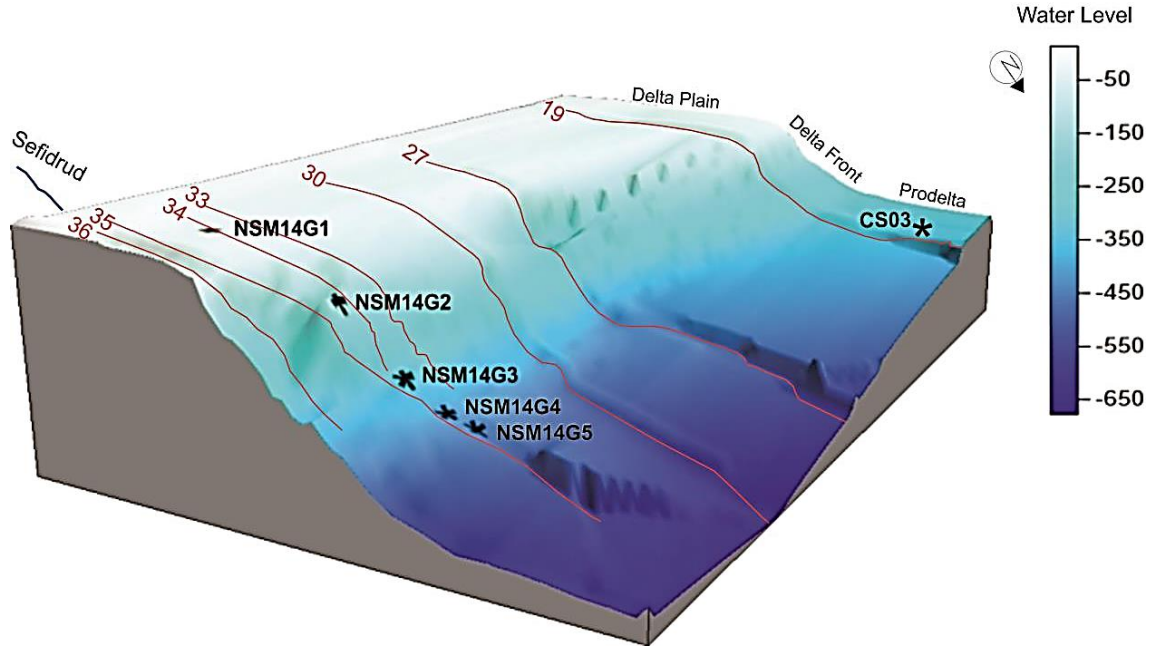


Figure 5- Digital Elevation Model of the Sefidrud Delta in the study area. Red lines: seismic profiles, black stars: Core locations

Bottomsets

The distal delta front gradually changes into the prodelta to form the third part, where the gradient is reduced to 20° and deposition of sediments occurs as bottomsets. The bottomset beds (e.g. core NSM14G5) contains of dark greyish brown silt with up to 96% silt.

The magnetic susceptibility (MS) values of the offshore cores were extremely low and the fluctuations were hardly worth discussing, probably within the error bars. The topset beds (most proximal core: NSM14G1) had the highest values, reaching 1.5 (Figure 6). This is low when compared to other sequences offshore Sefidrud delta, and offshore the southern CS (Leroy et al., 2013a) where MS reaches 60 offshore Babolsar and 24 offshore Anzali (cores CS10 and CS03 in Figure 2A; Leroy et al., 2013a). As no corrections were made for volume, it should also be considered that the diameter of core for the offshore cores from this study (7 cm diameter) is even larger than the diameter of cores from the 2013 study (5 cm diameter). The organic matter stays constant proximal-to-distal, with a maximum of 8% in the bottomset (core NSM14G5). The amount of carbonate is also relatively constant along all sequences, reaching up 9%, in topset beds (e.g. NSM14G1) (Figure 6).

Morphology of the Sefidrud Delta (Southwest Caspian Sea): a tectonically-driven Gilbert delta

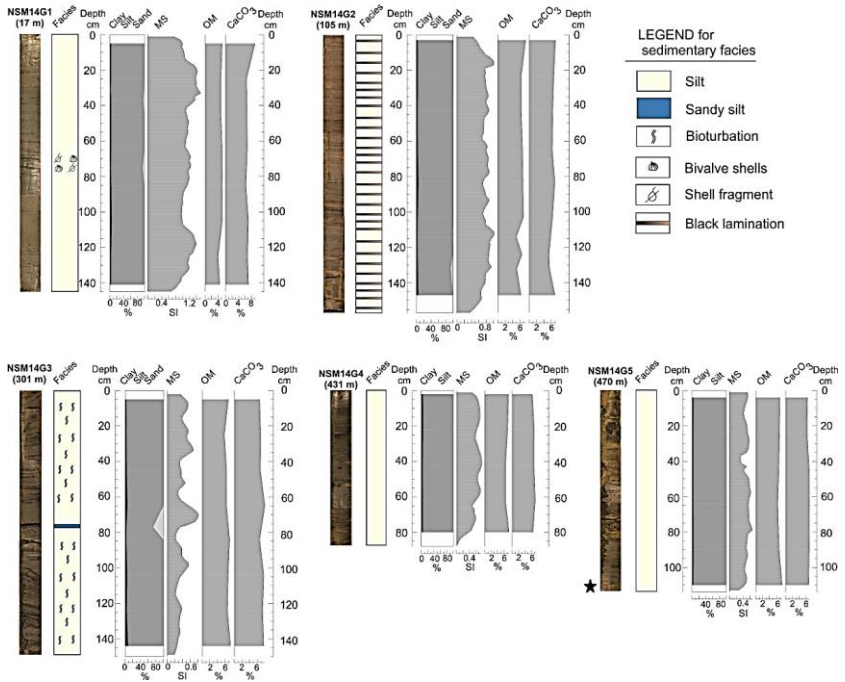


Figure 6- Sedimentary log for the marine sequence, displaying core photo and water depth in parentheses below the name of the core, sedimentary facies, grain size (clay, silt and sand), magnetic susceptibility (MS), organic matter (OM) and calcium carbonate (CaCO₃). The black star refers to the depth of the radiocarbon date.

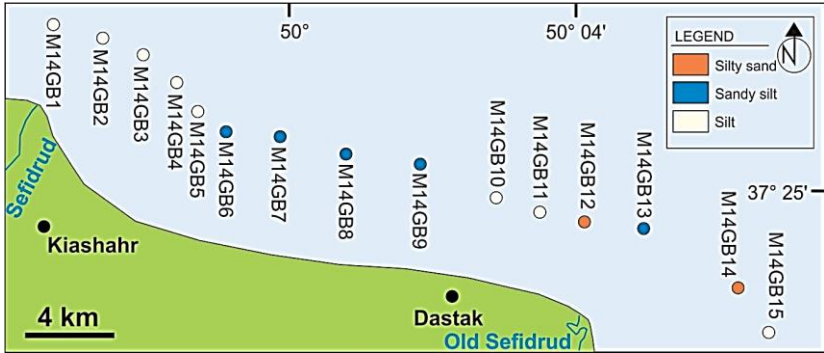


Figure 7- Distribution of silt, sandy silt and silty sand in surface samples from offshore.

4-3- Radionuclide and radiocarbon dating

The radionuclide results of core NSM14G3 show that ^{210}Pb values nearly reach background at 24 cm depth. The sedimentation rate for the top 9.5 cm is 1.65 mm yr⁻¹ and between 13 and 24 cm the sedimentation rate of 1.8 mm yr⁻¹ (Figure 8A). The lower sedimentation rate at the top corresponds to Manjil Dam construction upstream, which traps sediment (Haghani et al., 2016b). Between 9.5 and 13 cm, sedimentation rate is the lowest at 1.2 mm yr⁻¹. The record of artificial fallout ^{137}Cs also exhibits a roughly linear decreasing activity for the top 9.5 cm, followed by an increase between 9.5 and 13 cm and a decreasing activity for the samples between 13 and 24 cm (Figure 8B). The peak in ^{137}Cs curve corresponds to the peak in Pacific nuclear weapon testing around 1964. The best-fitted theoretical decay of ^{210}Pb is plotted in Fig. 8C, with a constant

sedimentation rate. If the sedimentation rate is considered to be constant, a sedimentation rate of 1.67 mm yr⁻¹ is obtained for the top 28 cm of sediment (Figure 8C). The very good correlation coefficient ($R^2=0.94$) confirms the lack of a sedimentary component between 9.5 and 13 cm depth. The base of the core could therefore be estimated to be at around AD 1120; thus, the sequence covers the last 900 years. The radiocarbon age for the base of core NSM14G5 is 885-690 BC (Table 3). Based on this, the sedimentation rate of this deeper core is 0.39 mm yr⁻¹ (Table 4).

Table 4-Sedimentation rates in the southern Caspian Sea. See figure 2A and 2E for the location of the cores programme version 7.1, with the Marine13 calibration curve (Reimer et al., 2013).

| Core name | Setting | Dating technique | Water depth (m) | Sedimentation rate (mm yr ⁻¹) | General age | References |
|-----------|---------------------------------|------------------|-----------------|---|------------------|---------------------|
| CS03 | Offshore Anzali | Radionuclide | 250 | 20 | Last centuries | Leroy et al., 2013a |
| US02 | Middle south basin | Radionuclide | 315 | 2 | Last millennium | Leroy et al., 2013a |
| 104 | Delta plain (sub-aerial) | Radiocarbon | 0 | 1.9 | Last millennium | This study |
| NSM14G3 | Offshore Sefidrud (delta front) | Radionuclide | 301 | 1.8 – 1.2 | Last millennium | This study |
| NSM14G5 | Offshore Sefidrud (prodelta) | Radiocarbon | 470 | 0.397 | Last millennia | This study |
| CP14 | Middle south basin | Radiocarbon | 330 | 0.2 | Early Holocene | Leroy et al., 2013b |
| GS05 | Middle south basin | Radiocarbon | 518 | 0.1 – 0.3 | Late Pleistocene | Leroy et al., 2013b |

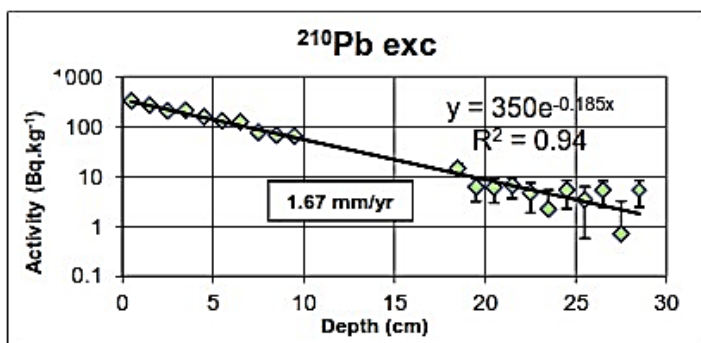
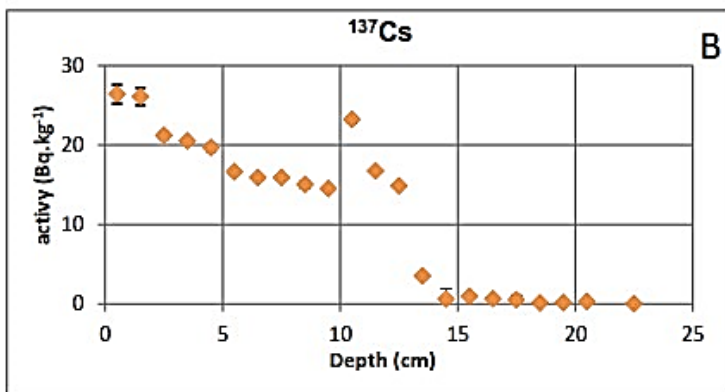
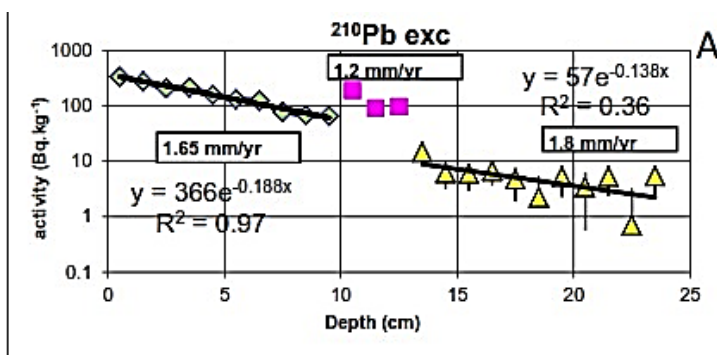


Figure 8- Radionuclide dating of core NSM14G3, based on CRS (constant rate of supply) model. (A): Profiles of ^{210}Pb activities (Bq kg^{-1} , dry weight) with depth in cm. The regression line corresponds to an average sedimentation rate of 1.67 mm/yr. (B): Profiles of ^{137}Cs activities (fallout from nuclear weapon testing) with depth in cm. (C): Radionuclide dating of core NSM14G3, based on constant sedimentation rate, Profiles of ^{210}Pb activities (Bq kg^{-1} , dry weight) with depth in cm

4-4- Macro-remains

NSM14G1

This sequence is dominated by faecal pellets (up to 62%), plant materials (up to 29%), foraminifers (up to 27) and bivalve shells (up to 46%). Moreover, shell fragments (11%), ostracod shells (up to 8%), charcoal (up to 2%) and gastropod shells (up to 0.3%) have been found in this sequence (Figure 9).

NSM14G2

Six various macro-remains have been observed in this sequence, including faecal pellets (up to 97%), plant materials (up to 20%), ostracod shells (up to 21%), charcoal (up to 7%), bivalve shells (up to 2%) and foraminifer tests (up to 3%) (Figure 9).

NSM14G3

This sequence is characterized by plant material (36%), charcoal (32%), faecal pellet (61%), clay flakes (33%), gastropod shells (up to 0.1%), bivalve shells (12%), ostracod shells (6%) and foraminifers (18%) (Figure 9).

NSM14G4

Based on the results on three samples taken in the top of sequence, up to 97% faecal pellets, 2% clay flakes, 0.9% charcoal, 32% plant material, 0.9% ostracod shells, 6% bivalve shells, 3% foraminifers and 0.8% shell fragments have been observed in this sequence (Figure 9).

NSM14G5

Seven different macro-remains have been observed in the nine samples taken in this sequence including clay flakes (up to 15%), faecal pellets (up to 84%), charcoal (up to 54%), plant materials (up to 38%), ostracod shells (up to 23%), bivalve shells (up to 4%) and foraminifers (up to 3) (Figure 9).

The highest absolute abundance (or concentration) of macro-remains occurs in core NSM14G5 at 65 cm (34083 counts per 10 g), with the number of faecal pellets reaching up to 28,545/10 g

(concentration diagram in Figure 9). The second highest peak belongs to core NSM14G5 at 20 cm where the number of faecal pellets reaches to $\sim 23,866/10$ g. The highest amount of foraminifer tests is observed in core NSM14G1 where ~ 2800 foraminifers/10 g were observed at 65 cm. Numbers of foraminifers remain considerably high in the cores NSM14G3, G4, and G5 where the water depth is quite deep (i.e. 301 m, 431 m, and 470 m, respectively (Figure 9). Two benthic species of foraminifers were identified in the sequence: *Ammonia beccarii* and *Elphidiella brotzkajae*. Although the limit for benthic foraminifer in the Caspian Sea is up to 70 m water depth and they become rare at the water depth greater than 25 m (Boomer et al., 2005; Leroy et al., under review).

Morphology of the Sefidrud Delta (Southwest Caspian Sea): a tectonically-driven Gilbert delta

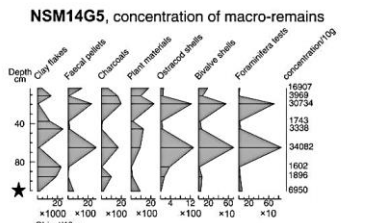
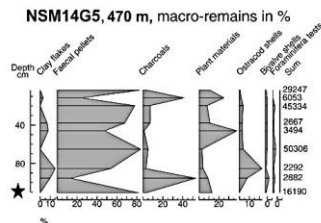
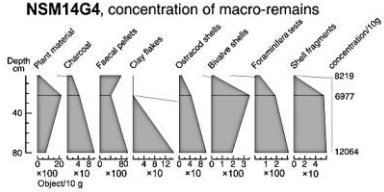
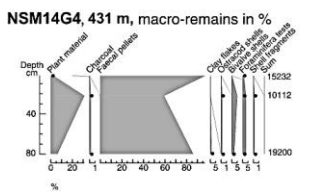
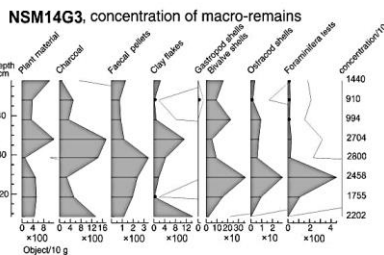
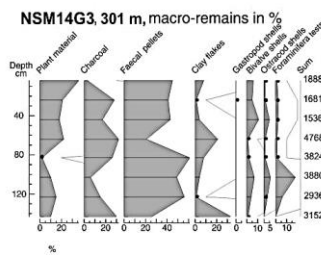
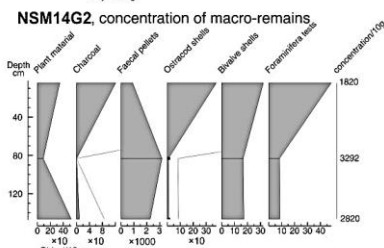
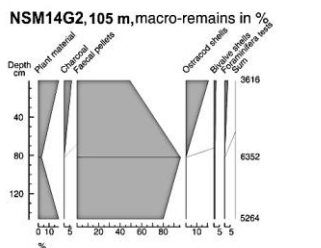
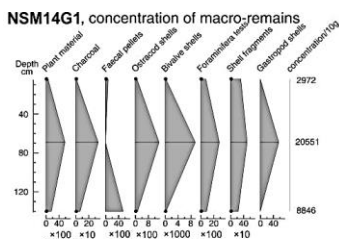
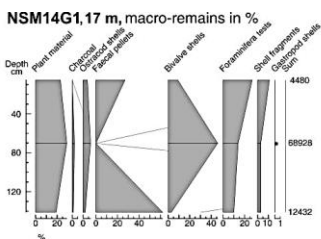


Figure 9- Macro-remains above 125 μ m of the five short offshore cores in percentages and concentration. The black dots represent very low percentages and concentration of macro-remains. The black star refers to the depth of the radiocarbon date.

4-5- Palynology

The concentration in pollen in the seven surface samples is good, between 5206 and 62,373 grains per ml. The pollen and NPP diagram indicate in the arboreal pollen (AP) the dominance of *Alnus*, *Carpinus betulus*, *Fagus* and *Quercus*. The non-arboreal pollen is dominated by *Amaranthaceae* (25-30%) with a significant presence of *Artemisia* and *Poaceae* (Figure 10A). *Alnus* is the most abundant in the deep sites, at 431 and 470 m depth. The *Asteraceae liguliflorae* and *Tubuliflorae*, the *Brassicaceae* and the *Cerealia* are the most important in the sample the closest to the Sefidrud mouth (M14GB1). Clearly this sample also shows a strong influence of river-transported palynomorphs with the high values of indeterminate and reworked pollen, fungal spores and *Glomus*. Some remarkable taxa are a grain of *Myrtaceae*, most likely derived from the plantation of *Eucalyptus* and the massula of exotic fern *Azolla filiculoides* used in the rice paddies (Leroy et al., 2011).

The pollen spectra reflect a mixture of sources: the Hyrcanian Forest (arboreal pollen with especially *Parrotia* and *Pterocarya*), the coastal plain (*Alnus* and

part of the *Amaranthaceae*), pollen grains transported from the Alborz Mountains and the Iranian Plateau (*Amaranthaceae* and *Artemisia* mostly) both by air and by water.

In the NPP, the typical open water taxa are the most abundant further offshore in the deeper than 300 m: *Anabaena*, *Pterosperma*, *Incertae sedis* 5b and 5d. *Botryococcus* is also most abundant in these deep samples. The dinocysts are well represented but their concentration varies widely from 626 (very poor) to 23,891 cysts per ml (very abundant). The dinocyst diagram shows a clear shift from a dominance by *Lingulodinium machaerophorum* in the three shallow sites (16 to 19 m) to an increase of *Impagidinium caspiense* in the sites deeper and further offshore (105 to 470 m). The foraminifer linings are well represented in the shallow sites (especially with a peak in the ample M14GB2); whilst the four deeper sites contain only rare remains. The P/D ratio of the two grab samples is very high, whilst in the other samples it drops, reflecting well the increasing distance to the coast. The same patterns are found in a transect from the coast to 221 m in the south-east of the Caspian Sea, with a shift between 25 and 46 m (Leroy et al., submitted).

On core NSM14G3, both the concentrations in pollen and in dinocysts are excellent (Figure 10B). The concentrations in pollen grains increase progressively from the bottom to the top, from 21,000 to 60,000 pollen grains/ml and are generally higher than in the surface

samples. The arboreal pollen (40%) is dominated by *Alnus* (22%). *Carpinus betulus*, deciduous *Quercus* and *Pinus* are frequent. *Fagus*, *Parrotia persica* and *Ulmus-Zelkova* are nearly continuously present. The non-arboreal types are dominated by *Amaranthaceae* (34%), *Artemisia* (17%) and *Poaceae* (6%). *Asteraceae Tubuliflorae* and *Cyperaceae* are frequent. Indicators of human activities are present, such as *Diospyros* (persimmon), *Juglans* (walnut), *Olea* (olive), *Camellia* (tea), *Vitis* (grape), *Cucumis* (cucumber or melon), *Cerealia* including *Secale* (rye), and perhaps *Urticaceae-Moraceae* (amongst others: mulberry), a well as coprophilous fungal spores. In the aquatic plants, *Typha-Sparganium* is regularly present. The monolet psilate spores are frequent above 113 cm (zones P-2 to P-4). The varia (indeterminable and reworked palynomorphs) are relatively abundant: 11%. The non-pollen palynomorphs (NPP) are largely dominated by *Incertae Sedis 5 b*, a possible Green algae, fungal spores, *Pterosperma* and *Anabaena*. Over the sequence the main changes are a peak of *Amaranthaceae* at the top (zone P-4), a drop of 5b at 123-113 cm and the overall drop of 5b, fungal spore, *Pterosperma*, *Anabaena* in the topmost sample.

The concentrations in dinocysts were the lowest at the core bottom: between 5800 and 6500 cysts per ml of wet sediment. They reached a maximum in the middle of the core between 103 and 64 cm depth around 34,000 cysts per ml, and fall slightly towards the top where they

are around 20,000 cysts per ml. The dinocysts assemblages are dominated by *Lingulodinium machaerophorum* B and *Impagidinium caspiense*. Less frequent other occurrences are *Brigantedinium*, *L. machaerophorum* ss, *Spiniferites cruciformis* A and some *Pentapharsodinium dalei*. Some Foraminifer inner organic linings are noted. The ratio P/D significantly fluctuates, with two periods of high values at the bottom (base of zone D-1 at 143-133 cm) and at the top of the sequence (zones D-3 and D-4).

The occurrence of the Green algae (5b and *Pterosperma*) and Cyanobacteria (*Anabaena*) are typical of offshore sequences. They drop significantly at 123-113 cm and at the top, following a similar pattern to P/D and an opposite pattern to *L. machaerophorum* B (Figure 10). This suggests two periods of shallower water.

4-6- Geochemical analysis

4-6-1- Siliciclastic proxies

Potassium (K) is normally associated with clay minerals (Koinig et al., 2003) and rubidium (Rb) can substitute K in both clay minerals and K-feldspars (Kylander et al., 2011). This is reflected in a strong correlation ($r_{K-Rb}=0.79$) between these two elements in core NSM14G5 (Figure 11). The correlation of K and Rb with Si and Al ($r_{K-Al}=0.86$; $r_{Rb-Si}=0.53$, Figure 11) also suggests that the source of the two alkali metals is mainly siliciclastic minerals.

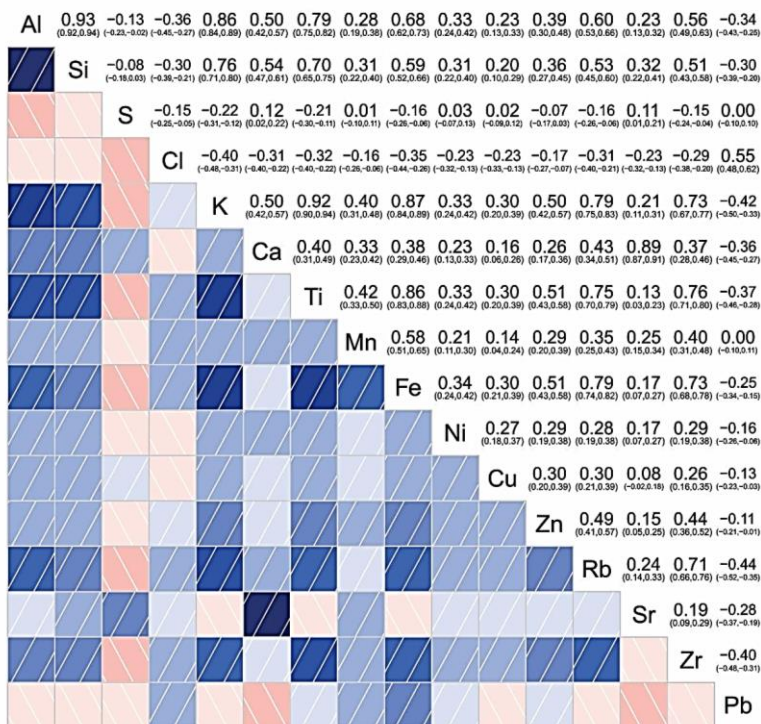


Figure 11- Pearson correlation matrix of elemental pairs on NSM14G5 sequence, blue colours and the rising linepattern indicate a positive correlation whereas red colours and the descending line pattern indicate negative values. The strength of correlation or anticorrelation increases with colour shades.

In a homogeneous sedimentation environment with negligible changes in grain-size distribution, Zr can be used for normalization as it is a conservative lithogenic element against which enrichment or

depletion processes can be analysed (Koinig et al., 2003). The sources of Zr are normally heavy minerals like zircon ($ZrSiO_4$) that are mainly found in coarser sediment fractions. In a heterogeneous sedimentation environment, Zr often shows a negative correlation with K and Rb, which are normally associated with clay minerals. As a result, the Zr/Rb ratio can be used an indicator for variations in grain-size distribution (Heymann et al., 2013; Unkel et al., 2014). Then, high Zr/Rb ratios reflect higher silt content (coarser), while lower ratios reflect more clay. Figure 12 shows hardly any variation of the Zr/Rb ratio along the core and both elements are highly correlated ($r_{Zr-Rb}=0.71$) supporting the very homogenous grain-size composition of core NMS14G5 (Figure 6). Silicon (Si) itself shows no specific development along the core. Measurements fluctuate around the overall Si-mean with the lowest values around 40 cm depth and the highest values shortly after around 30 cm (Figure 12).

4-6-2- Carbonate proxies

Calcium (Ca) enters the sediment usually as $CaCO_3$, i.e. calcite or aragonite (Cohen, 2003). It has either an allochthonous source from carbonate weathering in the catchment, or it autochthonously precipitates in the lake based on biogenic and/or chemical processes. Strontium (Sr) can be a substitute for Ca in carbonates and can co-precipitate with Ca forming carbonates from lake water (Cohen, 2003;

Kylander et al., 2011). Biogenic calcite precipitates mainly as aragonite and is more enriched in Sr than inorganically precipitated calcite/dolomite. Thus, Ca/Sr (Figure 12) is high when the contribution of detrital carbonate is elevated and the biogenic component is low (Hodell et al., 2008). Sr in association with plagioclase feldspars can also indicate an input of silicates to lake sediments (Kylander et al., 2011). The strong correlation of Sr with Ca ($r_{Sr-Ca}=0.89$) and the very low-correlation with siliciclastic proxies ($r_{Sr-Si}=0.32$) indicates the dominance of carbonate deposition as Sr source and only minor contributions from silicates in core NMS14G5.

A few distinct negative peaks in the Ca/Sr ratio occur at 95, 85, 40, 37.5, 12 and 2 cm depth in core NSM14G5, suggesting the dominance of biogenic processes at these levels. High concentration of Zr at 40 cm also suggests high input of heavy mineral and detrital input. Amongst these Ca/Sr peaks, the peaks at 40, 37.5 and 12 cm coincide with strong peaks in Cl-content that indicate higher salinities in comparison to the rest of the sequence.

Morphology of the Sefidrud Delta (Southwest Caspian Sea): a tectonically-driven Gilbert delta

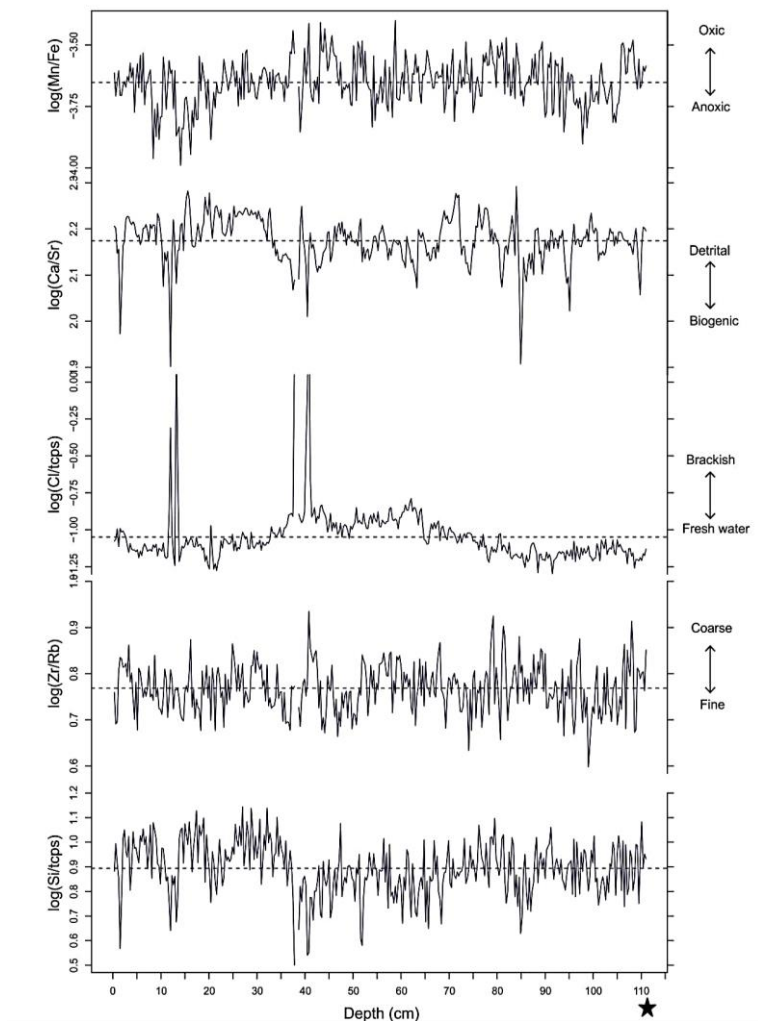


Figure 12- Environmental proxies from core NSM14G5: Mn/Fe ratio as indicator for oxic vs. anoxic; Ca/Sr ratio as indicator for detrital vs. biogenic carbonate input; Cl content as indicator of marine environment; Zr/Rb ratio as an indicator for grain size

distribution; Si content. The black star refers to the depth of radiocarbon date.

4-6-3- Iron and manganese

Changes in iron (Fe) and manganese (Mn) are quite difficult to interpret (Engstrom and Wright Jr, 1984) since a number of independent environmental factors control their supply and sedimentation, such as alkalinity, acidity (pH) and reduction potential (Eh). Nevertheless, the Mn/Fe ratio is often used as an indicator for redox conditions (Davison, 1993). As Fe_2^+ is less stable in more water than Mn_2^+ , it precipitates earlier than Mn_2^+ and hence Mn/Fe ratios in sediment are low when the sediment becomes anoxic (Koinig et al., 2003). In soil profiles, anoxic/reducing conditions are characterized by grey to blue colours (dominance of Fe_2^+), while oxic/oxidizing conditions are reflected by brown to red colours (dominance of Fe_3^+).

The Mn/Fe ratio shows no distinct trends or changes along the core (Figure 12). The longest, modest decreasing trend appears between approximately 45 and 15 cm depth. The peaks at 40, 37.5, and 12 cm with high Cl-content and low Ca/Sr ratios always coincide with maxima in the Mn/Fe ratio suggesting oxic and/or more alkaline conditions during these depositional events.

4-7- Radar profiles and sedimentary facies

In each radar profile, a core was taken to contribute to the interpretation. Grain analyses showed

that except the cores taken from profiles 106 and 107, the rest of the cores are dominated by sand and silty sand (Figure 13). A layer of organic-rich sediment was observed in the core from profile 104 (Figure 17, Appendix B), where the Kiashahr palaeo-beach is located. The organic-rich layer was barren in palynomorphs.

The penetration depth of the GPR signals reach only up to 4 m and decrease to 2 m in profiles 106 and 107 (Figure 13), due to fine-grain sediment deposition. Moreover, a limited depth of penetration of the GPR signal was expected in the study area due to the high-water table (Naderi Beni et al., 2013). High amount of silt/clay in some areas (i.e. profiles 106 and 107, Figure 2G & Figure 13) also contribute to signal attenuation (Jol and Smith, 1991; Jol et al., 1996). Gently dipping sigmoidal strata eastward and westward, with a maximum dip angle of 10° , were observed in profiles 123, 125, 104 and 105. The distinct sigmoidal shape of the internal pattern in these profiles suggests a prograding deltaic system, building out into the Caspian Sea (Figure 13). The only observed features in profiles 106 and 107 are multiples. In fact, fine sediments prevent the signal from penetrating through the layers and the only reflector (a clay/silt layer) is repeated in the image.

The data collected through GPR methods are highly subject to interpretation, especially if interferences are not identified correctly (Beres and

Haeni, 1991). Naderi Beni et al. (2013) conducted GPR survey to study the development of lagoons in the south Caspian Sea and some parts are interpreted as lagoonal deposits. However, the results from this study confirm that the GPR signal does not penetrate through fine sediments and therefore the lagoon deposits cannot be recorded in GPR profiles. GPR imaging of coastal deposits in sandy sediments is moderately successful in this study and provides useful data on the stratigraphy of coastal area. The strongly prograding system in the current shoreline (Figure 2E) and palaeo-shoreline (Figure 2F) indicates a high sedimentation supply relative to accommodation. Direction of sigmoidal records of progradation, also indicates movement of the deltaic system along the coastline.

From the sandy core taken on profile 104, where the palaeo-beach is located, two radiocarbon dates were obtained from two bivalve shells (*Cerastoderma glaucum*) at depths of 234 and 150 cm (Appendix B, Table 3 and Figure 2C). The deepest sample (at 234 cm) showed a very young age and the sample at 150 cm shows an age of AD1225, which provide a sedimentation rate of 1.9 mm yr⁻¹. The possibility of sand fallen from the wall during coring and the fact that the shells from 270 to 225 cm depth are not parallel and likely reworked from the upper parts of the sequence (Figure 16, Appendix A), makes us reject the lower date (at 234 cm). Radiocarbon dating and progradation pattern in profiles 104 and 105 (Figure 13) show that sediment supply was

high enough for rapid delta progradation into the basin, either at the time of deposition of the palaeo-beach (i.e. AD 1225), or at the present time.

Morphology of the Sefidrud Delta (Southwest Caspian Sea): a tectonically-driven Gilbert delta

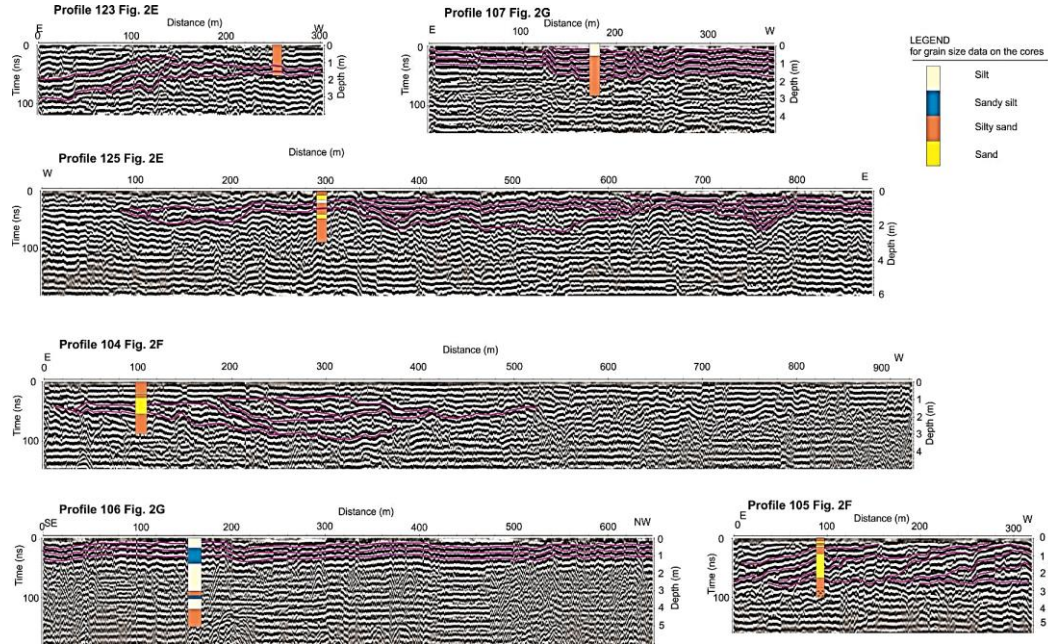


Figure 13- Ground Penetrating Radar (GPR) profiles from Sefidrud delta, for the location of the profiles see Fig. 2. Purple lines represent the main reflectors for interpretation. See appendix B for core descriptions.

5- Discussion

5-1- A Gilbert-like delta

The investigation of the delta subsurface, based on seismic profiles and cores indicate that the Sefidrud delta has a Gilbert-like, tripartite structure delta where a distinctive pattern of steeply-dipping delta front beds is sandwiched between horizontal delta plain and prodelta (Nichols, 2009). However, the steep foreset are controlled by fault system, rather than coarse sediments. The subaerial morphology of the prism displays a typical deltaic shape (Coleman and Wright, 1976). The Gilbert-type deltas can be found in three marine settings (Corner et al., 1990) including (1) tectonically active areas (Postma, 1984; Colella, 1988; Ori and Roveri, 1987), (2) fjord settings (Syvitski and Farrow, 1983; Postma and Cruickshank, 1988; Prior and Bornhold, 1988), (3) glaciodeltaic settings (McCabe et al., 1988). The common characteristics of this type of deltas are abundant supply of coarse materials, a relatively deep basin, and a sheltered low energy environment, causing relatively limited reworking of the sediments. Sefidrud Delta is located in a tectonically active area, where a fault system contributes to create the very steep slope of the delta front and allows for a vast accommodation space, which had resulted in exceptionally large accumulation rates during the Cenozoic (Brunet et al., 2003). However, a fundamental difference to the

classical definition of a Gilbert delta is the quasi absence of coarse sediment in the delta front and prodelta. Due to inland trapping of coarse sediments, the subaqueous part of the delta (topset) is fine grained. Indeed, the coarser sediments are dumped abruptly at the foot of the Alborz Mountains, due to a break of the slope as seen in the delta plain cores taken in Rostamabad (Fig. 2B; Sector I in Kazancı and Gulbabazadeh, 2013). Previous studies (Kazancı and Gulbabazadeh, 2013) suggested that the absence of coarse grain materials is due to dam construction in Manjil area in 1983, but considering the age of the offshore core in this study (NSM14G5) which shows a radiocarbon age of 690- 885 BC and the lack of coarse grain materials in the five offshore cores, suggest that other factors are involved. Therefore, the fine-grained nature of the topset is not only due to dam construction, but also due to the slope break at the foot of the Alborz Mountains. Indeed, the coarse fractions is trapped upstream in the flat delta plain (Fig. 2B). The sand materials are deposited mainly near to the new prism (e.g. BH1-1, 1-2, 47 and 51 in Fig. 4 Kazancı and Gulbabazadeh, 2011).

The delta plain is an erosional feature (fluvial and wave-cut platform), with a thin layer of sediments (topset beds), which produce considerable number of sediments eroded from this platform, and must have been redeposited not only by fluvial processes, but also by marine processes such as longshore currents. Together with river channel migration, this results in an arcuate

delta form. The layer containing shell fragments in proximal core (NSM14G1) is interpreted as turbidite. The delta plain evidently becomes replaced by narrow area of steep delta front which act as a bypass zone. Seismic data suggest the bottomset unit beneath the present distal prodelta area is c. 200 m thick (profile 30 in Figure 3). The delta is likely to be fed by hyperpycnal flows as the density of the CS is rather low with a salinity of only 13 psu.

5-2- Sedimentation rate and sediment delivery to the basin

Two models are mathematically practicable for calculating ^{210}Pb dates under varying sediment accumulation rates, the constant initial concentration (CIC) model and the constant rate of supply (CRS) model (Appleby and Oldfield, 1978; Robbins, 1978; Lubis, 2013). The constant initial concentration (CIC model) assumes that an increased flux of sedimentary particles from the water column will remove a proportionally increased amounts of ^{210}Pb from the water to the sediments. Whereas, the CRS model assumes that a constant fallout of ^{210}Pb from the atmosphere to the marine water takes place, resulting in a constant rate of supply of ^{210}Pb to the sediments irrespective of any variation that may have occurred in the sediment accumulation rate. Due to the large errors on the activity here, the CIC model was used to calculate the sedimentation rate. The decrease of ^{210}Pb with

depth is very regular from 9.5 cm depth to the top, which corresponds to a sedimentation rate of 1.65 mm yr⁻¹ with a correlation coefficient R² of 97%. Deeper in the core, i.e. between 24 and 13.5 cm, still about the same sedimentation rate (1.8 mm yr⁻¹) was observed, despite a R² of 36%. Between from 13.5 and 9.5 cm high activities of ²¹⁰Pb_{exc} was observed, probably due to a change in the sedimentation process. The sedimentation rate for the middle part was calculated as 1.2 mm yr⁻¹. The high activities measured between 13.5 and 9.5 cm would correspond to the same flux of radionuclides but with a lower dilution by a sedimentary component which deposited only with a sedimentation rate of 1.2 mm yr⁻¹. Higher sedimentation rate at the top and bottom of that section could be a result of mass-wasting events. Higher concentration of foraminifers in core NSM14G3 (301 m water depth) in comparison with the shallower cores (NSM14G1 and NSM14G2) is a sign of mass wasting of the sediments, since the foraminifer tests have to be transported to reach depth deeper than 50 m. It is necessary to note here that only benthic foraminifers were observed in the sequence (*A. beccarii* and *E. brotzkajae*) which can survive only down to 50 to 70 m water depth (Boomer et al., 2005; Leroy et al., under review). All ostracods in the Caspian Sea are benthic as well. Therefore, the foraminifers and ostracods in this sequence were reworked to deep basin and cannot be considered as water level indicator.

Sedimentation rate decreases proximal-to-distal from 1.9 mm yr⁻¹ in the deltaplain, followed by 1.8 to 1.2 mm yr⁻¹ in the deltafront and 0.39 mm yr⁻¹ in the prodelta (Table 4). This is in agreement with the Kura delta, where a higher sedimentation rate was reported at delta front in comparison to prodelta (Hoogendoorn, 2006). The rate of sedimentation in prodelta (e.g. 0.39 mm yr⁻¹ in NSM14G5) is around 50 times lower than a sedimentation rate in an offshore sequence taken from prodelta, near to the boundary of Sefidrud delta (20 mm yr⁻¹ in CS03, 250 m water depth, in Figure 2A, Figure 4 and Figure 5; Leroy et al., 2013a). This sedimentation rate is lower than the sedimentation rate in an offshore sequence in the middle of South Caspian basin (i.e. 2 mm yr⁻¹ in core US02, 315 m water depth, in Leroy et al. (2013a)) (Figure 2A for location of the core, Table 4). The huge difference between sedimentation rates in CS03 and NSM14G5 and NSM14G3 can be explained by the very steep continental shelf in the present study area. Indeed, due to the steep slope of the shelf, core NSM14G3 and NSM14G5 locations act as a bypassing zone and plumes continue carrying the sediments far from the river mouth until the plume loses momentum and the sediments accumulates into the basin (Figure 5). However, in core CS03 that was taken from the area with gentle slope, a higher sedimentation can occur (Figure 5). It should be noted that source of sediments in this part of the basin (the south Caspian basin) can be from western and northern rivers, which are distributed by wave-induced longshore currents. The sedimentation rate

in the basin can be compared with the sedimentation rates in the lagoonal area (Table 4 in Haghani et al., 2016b). Leroy et al. (2013a, b) discussed that the sedimentation rates in the lagoonal cores are higher than the sedimentation of those in the open sea. However, it should be taken in consideration in which part of the basin the cores are taken with the possibility of losing top core sediments up to 1 m (See Fig. 8 in Leroy et al., 2013b). In such cases (but not here) the absence of a clear peak of ^{137}CS in radionuclide results could mean that some loss occurred during core penetration. This should be considered when calculating sedimentation rates.

5-3- Indicators of water level changes

Although Gilbert deltas are renown to be excellent relative sea-level changes recorders (Gobo et al., 2015), few direct waters level indicators are found here owing to the lack of penetration of the geophysical data obtained here. Moreover, any observed change will have to take in consideration the compounding impact of the shift of the Sefidrud main distributary between the Old Sefidrud and the new Sefirud (Kousari, 1986; Krasnozhon et al., 1999; Lahijani et al., 2009; Leroy et al., 2011; Kazancı and Gulbabazadeh, 2013; Naderi Beni et al., 2013b; Haghani and Leroy, 2016) and the relatively low amplitude of the water level changes (10 m) in the last 3000 years.

Some indication of water levels may be found in palynology and macro-remains of core NSM14G3 and geochemistry of core NSMG5. The radionuclide dating on core NSM14G3 suggested a sedimentation rate of 1.67 mm yr⁻¹ and the radiocarbon dating on the base of NSM14G5 suggested a slower rate of sedimentation (i.e. 0.39 mm yr⁻¹). The proxies from these two cores are fitting very well to each other, and three periods of low-stands and two periods of high-stands were identified (Figure 14 & Figure 15).

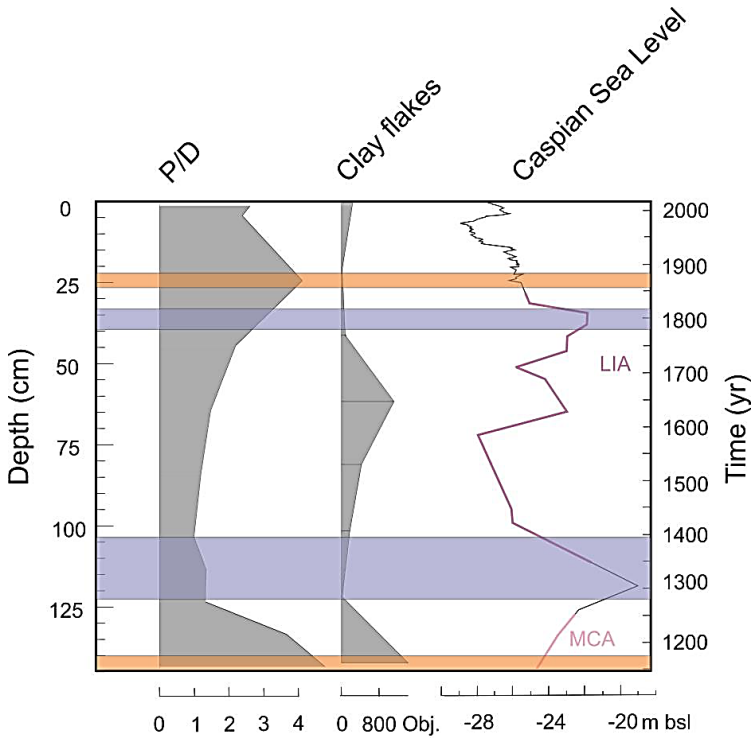


Figure 14- Palynology and Macro-remains from the NSM14G3 against Caspian Sea Level, the data from 1100 to 1900 from Naderi Beni et al. (2013); 1900 to 1992 from Lepeshevkov et al. (1981); 1992 to 2016 from USDA (2017). Orange and blue ribbons represent periods of low-stands and high-stands, respectively.

Three low stands

For the first clear lowstand, the best indicator is the high P/D ratio (suggesting proximity of the continent) at 143.5 cm with a small peak of *Brigantedinium* at 143.5-133.5 cm. This result is in agreement with macro-remain results, where the high

concentration of clay flakes (high erosion rate) suggests sea level fall. These clay flakes commonly form during relative sea-level fall and sea-level lowstand, when large areas of marine sediments are sub-aerially exposed (Allen and Allen, 2013). Additional scanty information comes from the same pollen zone (zone P-1) where more signs of erosion are recorded (reworked pollen, more fungal spores including *Glomus*, and occurrence of *Pseudoschizaea*). The erosion is best explained as a result of sea level fall and Sefidrud delta progradation. Considering the dating and the sedimentation rates, this corresponds to AD 1155, which is in agreement to the MCA low level (Figure 14). This period of low stand corresponds to very high log [Cl], at 40 and 37.5 cm at NSM14G5, with low log [Ca/Sr], and high log [Mn/Fe] values (Figure 15). The causes are either due to (1) a decrease in freshwater supply due to a shift away of the main hypopycnal flow from the main pathway of freshwater input or (2) a water level fall, leading to delta progradation into the sea. Lack of lamination, oxic condition (supported by high log [Mn/Fe]), and a small drop in magnetic susceptibility were also observed in this part of the sequence, supporting better ventilation. Low log [Ca/Sr] could be due to more development of biogenic material due to sea level fall, or more biogenic material reworked from lower water depth due to delta progradation. This is in agreement with observation of reworked bivalves, ostracods and foraminifers in deep part of the basin. This period of low water levels could also correspond to the higher values of clay flakes at 60

cm (Figure 15). The maximum peak of Zr (Figure 15) and deposition of sand (Figure 6) around 40 cm suggests high heavy mineral input due to delta progradation, during the low stand period.

The fairly high P/D ratio at 24.5 cm would suggest another clear period of low water levels. This corresponds to AD 1878, fitting to the low levels after AD 1850 (Figure 14).

High log Cl at 12 cm (Figure 15) represents another period of low water levels at AD 1712, where more oxic environment was supported by high log [Mn/Fe] in geochemical data. High log [Ca/Sr] suggests more detrital input due to delta progradation.

Two high stands

The first highstand is weakly marked by low values of the P/D ratio and of clay flakes (delta retrogradation) at 123 to 103 cm (NSM3). This is in a relatively good agreement with c. AD 1300, a highstand in the first part of the LIA (Figure 14). Low value of log [Cl] and high log [Ca/Sr] were observed in core NSM14G5 (Figure 15).

In the second highstand, lower concentrations of clay flakes at 35 cm are observed in NSM14G3 (Figure 14), which corresponds to the years AD 1800 in agreement with the late LIA high stand (Figure 14).

Lower log [Cl] values (more freshwater) and higher log [Ca/Sr] (high detrital) occurred in NSM14G5 (Figure 15), which suggest higher detrital input during period of sea level rise.

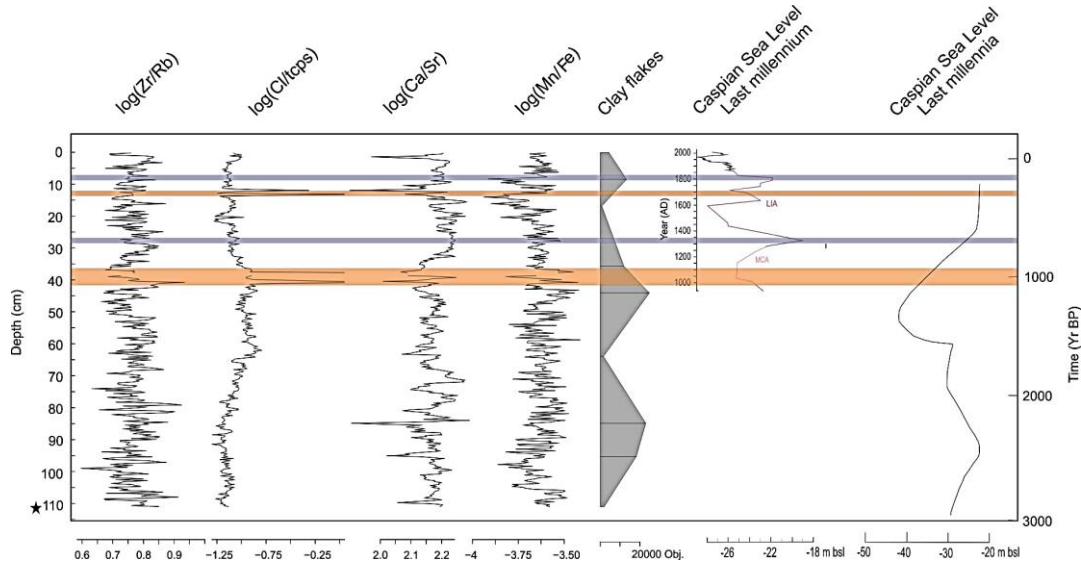


Figure 15- Geochemical and Macro-remains plot, from NSM14G5 against Caspian Sea Level, for the Caspian Sea Level during last millennium: the data from 1100 to 1900 from Naderi Beni et al. (2013); 1900 to 1992 from Lepeshevkov et al. (1981); 1992 to 2016 from USDA (2017). Orange and blue ribbons represent periods of low-stands and high-stands, respectively. The Caspian Sea Level during last millennia from Kroonenberg et al. (2008).

6- Conclusions

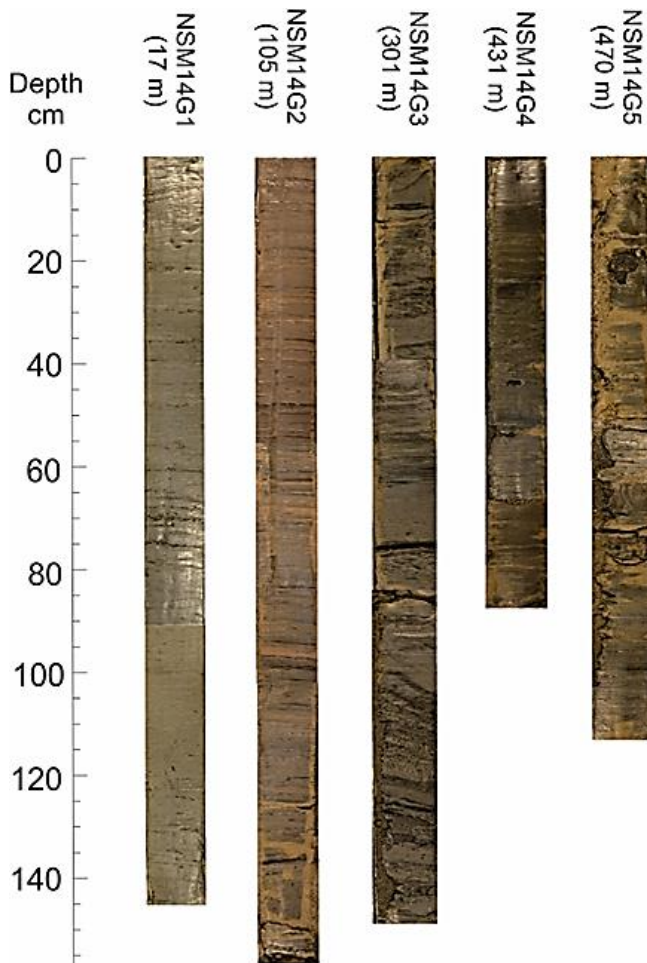
The modern Sefidrud delta features a pronounced Gilbert-like fan delta, controlled tectonically, with finer sediment than traditional Gilbert deltas. Analysis of aerial and subaqueous components reveals three distinct units: the subaqueous delta plain, delta front, and prodelta, indicative of Gilbert-like sedimentation. Sand accumulates on the aerial delta plain as the river exits the mountains. Further down, steeply angled delta front deposits suggest fault-driven slopes, likely related to the Khazar fault, which limit sediment deposition and result in low sedimentation rates. Both offshore and onshore areas exhibit significant accommodation space. Seismic profiles on the upper shelf show thin horizontal layers (approximately 7 m) overlying seaward-dipping layers at depths of 35-50 m, where the shelf break occurs. The unconformity surface is deep enough that historical Caspian Sea levels did not impact sedimentation, while the Sefidrud avulsion significantly altered sediment supply in the new area. Available accommodation space is filled by sediments prograding from the aerial and subaqueous delta plain into the delta front. Sedimentation rates decline sharply from 1.9 mm yr⁻¹ in the subaerial delta plain to 1.8-1.2 mm yr⁻¹ in the delta front, reaching 0.9 mm yr⁻¹ in the prodelta. Key factors influencing development include: (1) an abundant supply of coarse materials in the aerial delta and a scarcity in the subaqueous part, and (2) a steep slope at the river mouth, controlled by a fault system, which created a deep

depositional basin that promotes relatively high sedimentation rates influenced by fluvial and wave-induced longshore currents. However, the steep slope limits high sedimentation rates compared to the lower slopes at the delta boundary. Palynological, macroremains, and geochemical data indicate highstands during the late LIA and around AD 1300, leading to delta retrogradation, while lowstands during the MCA and parts of the LIA prompted delta progradation and increased coastal erosion. This study offers new insights into the evolving patterns of subaqueous sediment dispersal in Gilbert-like deltaic systems. The interaction between fluvial processes and marine influences is pivotal in understanding the dynamics of modern Sefidrud delta formation. The interplay of sediment supply from the river and the reworking by wave action shapes the morphological characteristics of the deltaic environment. The complex layer stratigraphy observed through seismic profiles suggests not only variations in sedimentation rates but also shifts in depositional regimes over time, reflecting the response of the delta to varying climatic and tectonic conditions. Furthermore, numerical simulations of sediment transport within the delta system could provide deeper insights into the sediment dispersal mechanisms at play. By integrating hydrodynamic models with sedimentological data, researchers can better interpret the spatial distribution of sediment and predict future changes in delta morphology. The sensitivity of the Gilbert-like fan delta to external controls such as sea level change and tectonic

activity further underscores the necessity for ongoing monitoring and modeling efforts. The role of biological factors, such as vegetation on the delta plain, cannot be overlooked as it contributes to sediment stabilization and impacts erosion rates. Root systems of terrestrial flora work synergistically with sediment deposition processes, enhancing soil retention and influencing the hydrological cycle within the delta. The feedback mechanisms between biotic and abiotic components present additional layers of complexity to the coastal ecosystem, suggesting that ecological health will play a crucial role in shaping sediment dynamics.

In conclusion, the Sefidrud delta exemplifies a dynamic system shaped by a myriad of factors, including geological, hydrological, and ecological processes. Continuous research efforts that incorporate advanced remote sensing technologies, sediment tracers, and multi-proxy paleoenvironmental data are essential to unraveling the intricate history and future trajectory of this deltaic system. Understanding these evolving patterns of sediment dispersal not only provides a framework for academic inquiry but also informs effective management strategies for coastal resilience in the face of global climatic changes.

Appendix A. Core photos (photo by S. Haghani). The number in bracket is water depth.



Figure

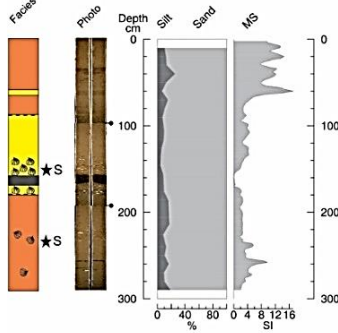
16:

Appendix

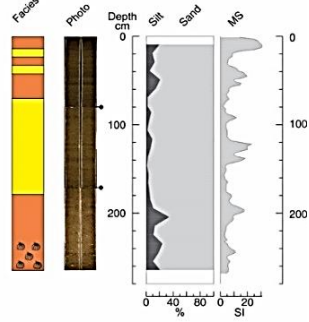
A

Appendix B

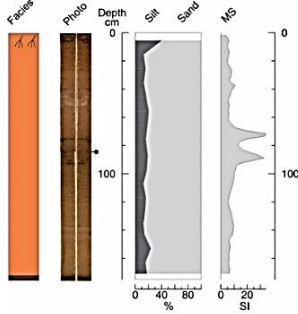
B1, Core 104



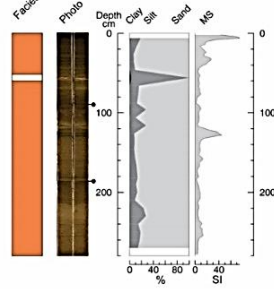
B2, Core 105



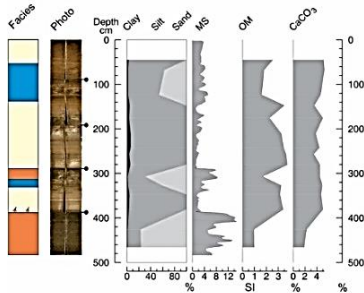
B3, Core 123



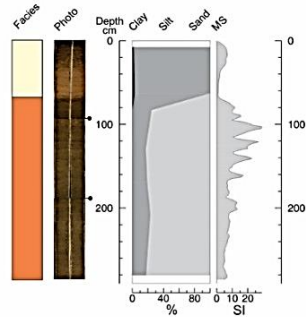
B4, Core 125



B5, Core 106



B6, Core 107



LEGEND for sedimentary facies

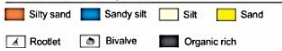


Figure 17: Appendix B: Sedimentary log for cores taken on GPR profiles, displaying sedimentary facies, sedimentary zone, core photo, grain size (clay, silt and sand) and magnetic susceptibility (MS). The black pin symbols show the core section limits. Black stars show the location of the dated samples.

Reference:

- Allen, P.A., Allen, J.R., 2013. Basin analysis: Principles and application to petroleum play assessment. John Wiley & Sons.
- Appleby, P.G., Oldfield, F., 1978. The calculation of lead-210 dates assuming a constant rate of supply of unsupported ^{210}Pb to the sediment. *Catena* 5 (1), 1-8.
- Arpe, K., Leroy, S., Wetterhall, F., Khan, V., Hagemann, S., Lahijani, H., 2014. Prediction of the Caspian Sea level using ECMWF seasonal forecasts and reanalysis. *Theoretical and Applied Climatology* 117, 41-60.
- Beres, M., Haeni, F. P., 1991. Application of Ground-Penetrating-Radar Methods in Hydrogeology Studies. *Groundwater* 29, 375-386.
- Birks, H.H., 2001. Plant macrofossils. In: Smol, J.P., Birks, H.J.B. and Last, W.M. (Eds.), *Tracking environmental change using lake sediments*. Springer, Netherlands pp. 49–74.
- Blott, S.J., Pye, K., 2001. GRADISTAT: a grain size distribution and statistics package for the analysis of unconsolidated sediments. *Earth surface processes and Landforms* 26 (11), 1237–1248.
- Boomer, I., von Grafenstein, U., Guichard, F., Bieda, S., 2005. Modern and Holocene sublittoral ostracod assemblages

(Crustacea) from the Caspian Sea: a unique brackish, deep-water environment. *Palaeogeography, Palaeoclimatology, Palaeoecology* 225 (1), 173-186.

- Bristow, C. S., 2009. Ground penetrating radar in aeolian dune sands. In: Jol, H., (Eds.), *Ground Penetrating Radar: Theory and Applications*. Amsterdam: The Netherlands, 273-297.
- Brunet, M.F., Korotaev, M.V., Ershov, A.V., Nikishin, A.M., 2003. The South Caspian Basin: a review of its evolution from subsidence modelling. *Sedimentary Geology* 156 (1), 119-148.
- Cohen, A.S., 2003. *Paleolimnology: the history and evolution of lake systems*. Oxford University Press, New York.
- Colella, A., 1988. Fault-controlled marine Gilbert-type fan deltas. *Geology* 16 (11), 1031-1034.
- Corner, G.D., Nordahl, E., Munch-Ellingsen, K., Robertson, K.R., 1990. Morphology and sedimentology of an emergent fiord-head Gilbert-type delta: Alta delta, Norway. *Coarse-Grained Deltas (Special Publication 10 of the IAS)* 27, 155-168.
- Cuven, S., Francus, P., Lamoureux, S., 2011. Mid to Late Holocene hydroclimatic and geochemical records from the varved sediments of East Lake, Cape Bounty, Canadian High Arctic. *Quat. Sci. Rev.* 30, 2651–2665. doi: 10.1016/j.quascirev.2011.05.019

- Davison, W., 1993. Iron and manganese in lakes. *Earth-Science Rev.* 34, 119–163. doi:10.1016/0012-8252(93)90029-7
- Djamour, Y., Vernant, P., Bayer, R., Nankali, H.R., Ritz, J.F., Hinderer, J., Hatam, Y., Luck, B., Le Moigne, N., Sedighi, M., Khorrami, F., 2010. GPS and gravity constraints on continental deformation in the Alborz Mountain range, Iran. *Geophysical Journal International* 183 (3), 1287-1301.
- Engstrom, D.R., Wright Jr, H.E., 1984. Chemical stratigraphy of lake sediments as a record of environmental change, in: Haworth, E.Y., Lund, J.W.G. (Eds.), *Lake Sediments and Environmental History: Studies in Palaeolimnology and Palaeoecology in Honour of Winifred Tutin*. Leicester University Press, Leicester, p. 411.
- Gobo, K., Ghinassi, M. and Nemec, W., 2015. Gilbert-type deltas recording short-term base-level changes: Delta-brink morphodynamics and related foreset facies. *Sedimentology* 62 (7), 1923-1949.
- Haghani, S., Leroy, S., 2016. Differential impact of long-shore currents on coastal geomorphology development in the context of rapid sea level changes: the case of the Old Sefidrud (Caspian Sea), *Quaternary International* (408), 78-92.
- Haghani, S., Leroy, S., under review. River response to relative water level fall: a major avulsion case from the Sefidrud (South West Caspian Sea), Submitted to *Geomorphology*, Oct 2016.

- Haghani, S., Leroy, S., Khdir, S., Kabiri, K., Naderi Beni, M., Lahijani, H.A.K., 2016a. An early Little Ice Age brackish water invasion along the south coast of the Caspian Sea (sediment of Langarud wetland) and its wider impacts on environment and people. *The Holocene* 26 (1), 3-16.
- Haghani, S., Leroy, S., Wesselingh, F., Rose, N., 2016b. Rapid evolution of coastal lagoons in response to human interference under rapid sea level change: A south Caspian Sea case study, *Quaternary International* (408), 93-112.
- Heiri, O., Lotter, A.F. and Lemcke, G., 2001. Loss on ignition as a method for estimating organic and carbonate content in sediments: reproducibility and comparability of results. *Journal of Paleolimnology* 25 (1), 101–110.
- Heymann, C., Nelle, O., Dörfler, W., Zagana, H., Nowaczyk, N., Xue, J., Unkel, I., 2013. Late Glacial to mid-Holocene palaeoclimate development of Southern Greece inferred from the sediment sequence of Lake Stymphalia (NE-Peloponnese). *Quat. Int.* 302, 42–60. doi:10.1016/j.quaint.2013.02.014
- Hodell, D.A., Channell, J.E.T., Curtis, J.H., Romero, O.E., Röhl, U., 2008. Onset of “Hudson Strait” Heinrich events in the eastern North Atlantic at the end of the middle Pleistocene transition (~640 ka)? *Paleoceanography* 23, PA4218. doi:10.1029/2008PA001591

- Hoogendoorn, R.M., 2006. The impact of changes in sediment supply and sea-level on fluvio-deltaic stratigraphy. Delft, Delft University of Technology, 153 pp., PhD Thesis.
- Jelinowska, A., Tucholka, P., Badaut-Trauth, D., 1999. Magnetic Mineral variation of south Caspian Sea sediments at laminate scale. *Physics and Chemistry of the Earth* 24 (9), 823-828.
- Jol, H. M., Smith, D. G., Meyers, R. A., 1996. Digital Ground Penetrating Radar (GPR): A new geophysical tool for coastal barrier research (examples from the Atlantic, Gulf and Pacific coasts, USA). *Journal of Coastal Research* 12 (4), 960-968.
- Jol, H.M., Smith, D.G., 1991. Ground penetrating radar of northern Lacustrine deltas. *Journal of Earth Sciences* 28, 1939–1947.
- Koinig, K.A., Shotyk, W., Lotter, A.F., Ohlendorf, C., Sturm, M., 2003. 9000 years of geochemical evolution of lithogenic major and trace elements in the sediment of an alpine lake – the role of climate, vegetation, and landuse history. *J. Paleolimnol.* 30, 307–320. doi:10.1023/A:1026080712312
- Kosarev, A.N. and Kostianoy, A.G., 2005. The Caspian Sea environment: The Handbook of Environmental Chemistry. Springer Science and Business Media
- Kousari, S., 1986. Evolution of Sefidrud Delta, Development in *Geological Education* 1, 31–41 (in Persian).

- Krasnozhon, G.F., Lahijani, H., Voropayev, G.V., 1999. Evolution of the delta of the Sefidrud River, Iranian Caspian Sea coast, from space imagery. *Mapping Science and Remote Sensing* 36, 256-264.
- Kroonenberg, S.B., Abdurakhmanov, G.M., Badyukova, E.N., et al., 2007. Solar-forced 2600 BP and Little Ice Age highstands of the Caspian Sea. *Quaternary International* 173, 137–143.
- Kroonenberg, S.B., Kasimov, N.S., Lychagin, M.Y., 2008. The Caspian Sea, a natural laboratory for sea-level change. *Geography, Environment, Sustainability* 1 (1), 22-37.
- Kroonenberg, S. B., Rusakov, G. V., Svitoch, A. A., 1997. The wandering of the Volga delta: a response to rapid Caspian Sea-level change. *Sedimentary Geology* 107 (3), 189-209.
- Kylander, M.E., Ampel, L., Wohlfarth, B., Veres, D., 2011. High-resolution X-ray fluorescence core scanning analysis of Les Echets (France) sedimentary sequence: new insights from chemical proxies. *J. Quat. Sci.* 26, 109–117. doi:10.1002/jqs.1438
- Lahijani, H.A.K., Tavakoli, V., Amini, A.H., 2008. South Caspian River mouth configuration under human impact and sea level fluctuations. *Environmental Sciences* 5, 65–86.
- Lahijani, H.A.K., Rahimpour-Bonab, H., Tavakoli, V., Hosseindoost, M., 2009. Evidence for late Holocene highstands in central Guilan–East Mazanderan, south

Caspian coast, Iran. *Quaternary International* 197 (1), 55-71.

Leroy, S., Chalié, F., Wesselingh, F., Sanjani, S., Lahijani, H., Athersuch, J., Struck, U., Plunkett, G., Reimer, P., Habibi, P., Kabiri, K., Haghani, S., Naderi Beni, A., Arpe, K., 2016. Multi-proxy indicators in a Pontocaspian system: a depth transect of surface sediment in the S-E Caspian Sea. Submitted.

Leroy, S., Lahijani, H., Reyss, J., Chalié, F., Haghani, S., Shah-Hosseini, M., Shahkarami, S., Tudryn, A., Arpe, K., Habibi, P., 2013a. A two-step expansion of the dinocyst *Lingulodinium machaerophorum* in the Caspian Sea: the role of changing environment. *Quaternary Science Reviews* 77, 31–45.

Leroy, S. A., Tudryn, A., Chalié, F., López-Merino, L., Gasse, F., 2013b. From the Allerød to the mid-Holocene: palynological evidence from the south basin of the Caspian Sea. *Quaternary Science Reviews* 78, 77-97.

Lepeshevkov IN, Buynevich DV, Buynevich NA et al., 1981. Perspectives of Use of Salt Resources of Kara-Bogaz-Gol. Moscow: Academia Nauka, p. 273 (in Russian).

Lövemark, L., Chen, H.F., Yang, T.N., Kylander, M., Yu, E.F., Hsu, Y.W., Lee, T.Q., Song, S.R., Jarvis, S., 2011. Normalizing XRF-scanner data: A cautionary note on the interpretation of high-resolution records from organic-rich lakes. *J. Asian Earth Sci.* 40, 1250–1256. doi:10.1016/j.jseaes.2010.06.002

- Lubis, A. A., 2013. Constant rate of supply (CRS) model for determining the sediment accumulation rates in the coastal area using ^{210}Pb . *Journal of Coastal Development* 10 (1), 9-18.
- McCabe, A.M. and Eyles, N., 1988. Sedimentology of an ice-contact glaciomarine delta, Carey Valley, Northern Ireland. *Sedimentary Geology*, 59 (1-2), 1-14.
- Mazzullo, J.M., Meyer, A., and Kidd, R., 1988. New sediment classification scheme for the Ocean Drilling Program. In: Mazzullo, J.M. and Graham, A.G. (Eds.), *Handbook for shipboard sedimentologists*. ODP Technical Notes 8, 45–67.
- Milliman, J., Haq, B.U., 1996. *Sea-level rise and coastal subsidence: causes, consequences, and strategies* (Vol. 2). Springer Science & Business Media.
- Naderi Beni, A., Lahijani, H., Harami, R.M., Leroy, S.A.G., Shah-Hosseini, M., Kabiri, K. and Tavakoli, V., 2013. Development of spit-lagoon complexes in response to Little Ice Age rapid sea-level changes in the central Guilan coast, South Caspian Sea, Iran. *Geomorphology* 187, 11–26.
- Neal, A., 2004. Ground-penetrating radar and its use in sedimentology: principles, problems and progress. *Earth-science reviews* 66 (3), 261-330.
- Nichols, G., 2009. *Sedimentology and stratigraphy*. John Wiley and Sons.

- Ori, G.G., Roveri, M., 1987. Geometries of Gilbert-type deltas and large channels in the Meteora Conglomerate, Meso-Hellenic basin (Oligo-Miocene), central Greece. *Sedimentology* 34 (5), 845-859.
- Postma, G., 1984. Slumps and their deposits in fan delta front and slope. *Geology* 12 (1), 27-30.
- Postma, G., Cruickshank, C., 1988. Sedimentology of a late Weichselian to Holocene terraced fan delta, Varangerfjord, northern Norway. *Fan deltas: Sedimentology and tectonic settings*, 144-157.
- Preoteasa, L., Vespremeanu-Stroe, A., Tățui, F., Zăinescu, F., Timar-Gabor, A., Cîrdan, I., 2016. The evolution of an asymmetric deltaic lobe (Sf. Gheorghe, Danube) in association with cyclic development of the river-mouth bar: Long-term pattern and present adaptations to human-induced sediment depletion. *Geomorphology* 253, 59-73.
- Prior, D.B. and Bornhold, B.D., 1988. Submarine morphology and processes of fjord fan deltas and related high-gradient systems: modern examples from British Columbia. *Fan deltas: sedimentology and tectonic settings*, 125-143.
- R Core Team, 2014. *R: A Language and Environment for Statistical Computing*.
- Reading, H. G., 2009. *Sedimentary environments: processes, facies and stratigraphy*. John Wiley and Sons.

- Reimer, P.J., Bard, E., Bayliss, A., Beck, J.W., Blackwell, P.G., Ramsey, C.B., Buck, C.E., Cheng, H., Edwards, R.L., Friedrich, M., Grootes, P.M., Guilderson, T.P., Haflidason, H., Hajdas, I., Hatté, C., Heaton, T.J., Hoffmann, D.L., Hogg, A.G., Hughen, K.A., Kaiser, K.A., Kromer, B., Manning, S.W., Niu, M., Reimer, R.W., Richards, D.A., Scott, E.M., Southon, J.R., Staff, R.A., Turney, C.S.M. and Plicht, J.V.D., 2013. IntCal13 and Marine13 radiocarbon age calibration curves 0–50,000 years cal BP. *Radiocarbon* 55 (4), 1869–1887.
- Reynolds, J.M., 1997, *An Introduction to Applied and Environmental Geophysics*, John Wiley and Sons, Chichester.
- Richter, T.O., van der Gaast, S., Koster, B., Vaars, A., Gieles, R., de Stigter, H.C., De Haas, H., van Weering, T.C.E., 2006. The Avaatech XRF Core Scanner: technical description and applications to NE Atlantic sediments. *Geol. Soc. London, Spec. Publ.* doi:10.1144/GSL.SP.2006.267.01.03
- Robbins, J.A., 1978. Geochemical and geophysical applications of radioactive lead. *The biogeochemistry of lead in the environment* 1, 285-337.
- Röhl, U., Abrams, L.J., 2000. High-resolution, downhole, and nondestructive core measurements from Site 999 and 1001 in the Caribbean Sea: Application to the Late Paleocene Thermal Maximum. *Proc. Ocean Drill. Program, Sci. Results* 165, 191–203.

- Selley, R. C., 1996. Ancient sedimentary environments and their sub-surface diagnosis. Chapman and Hall, London.
- Stanley, D.J., Warne, A.G., 1994. Worldwide initiation of Holocene marine deltas by deceleration of sea-level rise. *Science* 265, 228-231.
- Stuiver, M., Reimer, P.J., 1993. Extended 14C database and revised Calib 3.0 14C age calibration program. *Radiocarbon* 35, 215–230.
- Syvitski, J.P., Farrow, G.E., 1983. Structures and processes in bayhead deltas: Knight and Bute Inlet, British Columbia. *Sedimentary geology* 36 (2), 217-244.
- UNEP, 2006. Stolberg, F., Borysova, O., Mitrofanov, I., Barannik, V., Egtesadi, P. Caspian Sea, GIWA Regional assessment 23. University of Kalmar, Kalmar, Sweden.
- Unkel, I., Schimmelmann, A., Shriener, C., Forsén, J., Heymann, C., Brückner, H., 2014. The environmental history of the last 6500 years in the Asea Valley (Peloponnese, Greece) and its linkage to the local archaeological record. *Zeitschrift für Geomorphol. Suppl. Issues* 58, 89–107. doi:10.1127/0372-8854/2014/S-00160
- USDA, 2017. www.pecad.fas.usda.gov/cropexplorer/global_reservoir (last accessed 14.04.17).
- Weltje, G.J., Tjallingii, R., 2008. Calibration of XRF core scanners for quantitative geochemical logging of

sediment cores: Theory and application. *Earth Planet. Sci. Lett.* 274, 423–438. doi:10.1016/j.epsl.2008.07.054

Wright, K., 2014. R Corrgram Package, Version 1.6.

Wunderlich, J., Müller, S., 2003. High-resolution sub-bottom profiling using parametric acoustics. *International Ocean Systems* 7 (4), 6-11.

Yousefi Zoshk, R. Y., Mohammadi, K. B., Zeighami, M., Baghizadeh, S., Golcheh, M., Ahmadpour, H., Miri, J., Nezhad, M. G., Nezari, N., Mohammadi, N. B., Alimadadi, E., 2015. "MeymanatAbad Tepe: An important Site in Late Fourth Millennium BC in Iranian Central Plateau". *Archaeology*, 4 (1), pp. 13- 21.

Zomorrodian, M. J., 2002. *Geomorphology of Iran (Climatic Processes and External Dynamics, Mashhad, Ferdowsi University Publications, Mashhad, pp. 268, (In Persian).*

